Structural Basis for Membrane Targeting and Secretion of Legionella SidE Ubiquitin Ligases

Ivan Dikic

dikic@biochem2.uni-frankfurt.de

Goethe University https://orcid.org/0000-0001-8156-9511

Mohit Misra

University of Frankfrut https://orcid.org/0000-0001-6309-8066

Rukmini Mukherjee

Goethe University

Anshu Bhattacharya

Goethe University

Tsai-Hsuan Weng

Max Planck Institute of Biophysics https://orcid.org/0000-0002-3708-6384

Chuang Li

Purdue University

Wenbo Chen

MPI Biophysics

Larissa van Ek

University of Geneva https://orcid.org/0000-0002-8047-1560

Ahmed Mohammed

EMBL

Alberto Cristiani

Goethe Univeristy

Yaobin Liu

Goethe Univeristy

Julia Pomirska

Goethe Univeristy

Adela Vidov

Goethe Univeristy

Diana Grewe

Goethe Univeristy

Gerbrand van der Heden van Noort

Leiden University Medical Center https://orcid.org/0000-0001-5955-6431

Gerhard Hummer

Max Planck Institute of Biophysics https://orcid.org/0000-0001-7768-746X
Anne-Claude Gavin
University of Geneva https://orcid.org/0000-0003-4917-2340
Schara Safarian
MPI Biophysics
Zhao-Qing Luo
Purdue University West Lafayette https://orcid.org/0000-0001-8890-6621
Ramachandra Bhaskara
Goethe University https://orcid.org/0000-0002-7742-0391
Dmitri Svergun
EMBL
Misha Kudryashev
MPI Biophysics

Article

Keywords: LCV (Legionella containing vacuole), CTD (C-terminal domain), BAR (Bin amphiphysin-RvS), PR-ubiquitination(Phospho-ribose ubiquitination), DUB (DeUBiquitinase), PDE (Phosphodiesterase), mART (mono-ADP-ribosyl transferase), CC (Coiled coil), T4SS(Type IV secretion system)

Posted Date: May 13th, 2025

DOI: https://doi.org/10.21203/rs.3.rs-6524297/v1

Additional Declarations: There is **NO** Competing Interest.

Structural Basis for Membrane Targeting and Secretion of *Legionella* SidE Ubiquitin Ligases

Mohit Misra[1,2], Rukmini Mukherjee[2,3], Anshu Bhattacharya[1,2], Tsai-Hsuan Weng[3], Chuang Li[4], Wenbo Chen[1,2,3], Larissa C. van Ek[5], Ahmed Mohammed[6], Alberto Cristiani[1,2], Yaobin Liu[1,2], Julia Pomirska[1,2], Adela Vidov[1,2], Diana Grewe[1,2], Gerbrand van der Heden van Noort[7], Gerhard Hummer[3], Anne-Claude Gavin[5], Schara Safarian[3,8], Zhao-Qing Luo[4], Ramachandra M. Bhaskara[1,2], Dmitri Svergun[6], Misha Kudryashev[2,3,9] and Ivan Dikic*[1,2,3,8]

Affiliations:
[1] Goethe University Frankfurt, Medical Faculty, Institute of Biochemistry II, Theodor-Stern-Kai 7, 60590 Frankfurt am Main, Germany
[2] Goethe University Frankfurt, Buchmann Institute for Molecular Life Sciences, Max-von-Laue-str. 15, 60438 Frankfurt am Main, Germany
[3] Max Planck Institute of Biophysics, Max-von-Laue-str. 3, 60438 Frankfurt am Main, Germany
[4] Purdue Institute of Immunology, Inflammation and Infectious Diseases and Department of Biological Sciences, Purdue University, West Lafayette, IN, USA
[5] Department of Cell Physiology and Metabolism, Faculty of Medicine, University of Geneva, Rue Michel-Servet 1, 1211 Geneva, Switzerland
[6] European Molecular Biology Laboratory (EMBL) Hamburg Site, Hamburg, Germany
[7] Department of Cell and Chemical Biology, Leiden University Medical Center, Leiden, Netherlands
[8] Fraunhofer Institute for Translational Medicine and Pharmacology ITMP, Frankfurt/Main, Germany
[9] In Situ Structural Biology, Max-Delbrück-Center for Molecular Medicine in the Helmholtz Association (MDC), 13125, Berlin, Germany.

* Corresponding author dikic@biochem2.uni-frankfurt.de

Highlights:

The crystal structure of the SdeA CTD (C-terminal domain) reveals a BAR domain-like architecture

The CTD determines subcellular localization and substrate specificity of SidE effectors

An amphipathic helix within the CTD mediates membrane anchoring

The CTD contains distinct, mutually exclusive sites for membrane tethering and secretion via the Type IV secretion system

The SidE CTD is as critical for *Legionella* replication as the PR-ubiquitination activity

Abstract

SidE family effectors from *Legionella pneumophila* catalyze serine ubiquitination of host proteins via phospho-ribose (PR) linkages, disrupting host compartments, facilitating the formation of *Legionella*-containing vacuoles (LCVs) and blocking xenophagy. Upon infection, SidE proteins are injected into the cytosol and recruited to host membranes. Here we present structural and functional insights into a previously uncharacterized C-terminal domain (CTD) of SidE effectors. The crystal structure reveals a banana-shape resembling eukaryotic BAR-domain dimers, with an amphipathic helix and electropositive patch mediating membrane association. Membrane targeting to ER and Golgi confers substrate specificity for PR-ubiquitination. We further show that the CTD binds the IcmS-IcmW-DotL complex, acting as a secretion signal for the Type IV secretion system. Our findings establish membrane localization and secretion as critical determinants of SidE effector function during *Legionella* infection.

Keywords: LCV (*Legionella* containing vacuole), CTD (C-terminal domain), BAR (Bin-amphiphysin-RvS), PR-ubiquitination (Phospho-ribose ubiquitination), DUB (DeUBiquitinase), PDE (Phosphodiesterase), mART (mono-ADP-ribosyl transferase), CC (Coiled coil), T4SS (Type IV secretion system)

Main

Legionella pneumophila are Gram-negative intracellular pathogens responsible for diseases such as Legionnaires' disease and Pontiac fever[1–4]. Central to their virulence is a cohort of ~300 effector proteins translocated into host cells via the Type IV secretion system (T4SS). The Dot/Icm T4SS is multiprotein assembly which spans from the inner membrane to outer membrane and regulates the movement of toxins across bacterial membrane[5]. These effectors reprogram host pathways to create a replication-permissive niche while evading immune responses and xenophagy.

Many *Legionella* effectors are enzymatically diverse and functionally redundant due to gene duplication. Some operate in concert as para-effectors[6], while others function as meta-effectors[7–9], modulating or reversing earlier effectors' activities. This orchestrates a complex, temporal host-pathogen interaction network. A major strategy involves subverting host ubiquitin signaling[10,11]. Effectors such as SidC and SdcA act as E3 ligases[12–14], while others (RavD, LotA-D) serve as deubiquitinases (DUBs)[11,15–18], mimicking eukaryotic enzymes.

The SidE effector family, comprising SdeA, SdeB, SdeC, and SidE, features a unique combination of canonical DUB activity and non-canonical PR-ubiquitination[9,19–22]. Their shared domain architecture includes an N-terminal DUB (targeting K63-linked ubiquitin chains), a phosphodiesterase (PDE), and a mono-ADP-ribosyltransferase (mART) domain, which

together catalyze ADP-ribosylation of ubiquitin at R42 and its subsequent conjugation to host substrates [20,21]. However, the large CTD (~350–700 residues) has remained structurally and functionally uncharacterized.

We now reveal that the CTD adopts a BAR domain-like architecture with an amphipathic helix mediating membrane insertion. BAR-domains are prevalent in eukaryotes and form the largest group of membrane-sensing and bending proteins[23]. SidE CTD derived membrane targeting underlies SidE substrate specificity. Mutating this region abrogates localization to ER/Golgi and fails to rescue the ΔSidE growth defect in *Legionella*, despite intact enzymatic activity. Additionally, we demonstrate that the CTD mediates interaction with the IcmS-IcmW-DotL chaperone complex, serving as a secretion signal for T4SS translocation. Our findings close a major gap in understanding full-length SidE protein function, highlighting how CTD-mediated membrane targeting and secretion dictate effector localization and substrate engagement.

Results:

An Integrative Model of full-length SdeA/ SdeC combining Cryo-EM and Crystallography

Members of the SidE effector family from *Legionella pneumophila* exhibit a modular architecture in which the N-terminal half harbors three conserved enzymatic domains: DUB, PDE, and mART (Fig. 1a). These domains are highly conserved (70–88% identity) across family members, with the exception of the PDE in SdeC, which shares only 45% identity with SdeA. The C-terminal half is more variable, with coiled-coil regions exhibiting 44–92% identity and the uncharacterized CTD showing 37–63% identity. Phylogenetic analysis clusters SdeA and SidE as closely related, while SdeB and SdeC are more similar to each other.

Although a crystal structure of SdeA containing the PDE, mART, and coiled-coil domains has been previously reported[22], the large CTD (~40 kDa in SdeA, SdeB, SdeC; ~80 kDa in SidE) has not been structurally deciphered. To resolve the domain architecture, we purified full-length SdeC with N-terminal GST and C-terminal His tags and conducted cryo-EM analysis. Two datasets comprising 2,389 and 1,392 micrographs were collected on a Titan Krios microscope. After particle picking with Topaz and 2D classification, 1,071,832 particles were retained for 3D reconstruction. Subsequent CTF and local refinement yielded a 4.6 Å map from 186,225 particle, further improved to 4.1 Å using heterogeneous and non-uniform refinement (Fig. 1b).

We observed no EM density for the flexible DUB domain, likely due to a long linker between DUB and PDE. The CTD exhibited conformational heterogeneity, prompting focused refinement of the PDE-mART region, which yielded a 3.8 Å map (Ext. Fig. 1). A composite atomic model of SdeC was constructed using the available crystal structure of SdeA (PDB:

5YIM) and AlphaFold3 predictions[24]. While the CTD remained partially resolved (Ext. Fig. 2a), the catalytic core was modeled confidently (Ext. Fig. 2b, c). Notably, structural comparison of PDE domains from SdeA and SdeC revealed significant divergence, consistent with their 46% sequence identity. Unique insertions in SdeC and deletions relative to SdeA suggest differences in substrate recruitment (Ext. Fig. 2d). To capture dynamic flexibility, we performed normal mode analysis (NMA) of the cryo-EM data. The top three low-frequency modes accounted for the conformational diversity observed in 2D classes, indicating that the CTD-flexible hinge region governs large-scale motions (Ext. Fig. 3a, b).

Given the limited resolution of the CTD in cryo-EM, we turned to X-ray crystallography. The isolated CTD of SdeA was crystallized and the crystal diffracted to 2.0 Å resolution. Despite lacking homology to known folds, we solved the structure using single-wavelength anomalous dispersion (SAD) with ethyl mercury thiosalicylate (EMTS) soaking. The resulting structure revealed a banana-shaped structure formed by two helical lobes connected via a long α-helix (Fig. 1c), strongly reminiscent of eukaryotic BAR domains, which sense and remodel membranes. The N-terminal lobe contains α1, α2, α3, η1, α4 helices connected to the C-terminal lobe via a long α5 helix. The C-terminal lobe represents α6- α10 and η2 helices, whereas the last 15 residues were unresolved in the crystal structure. Structural overlay with the Arfaptin BAR domain (PDB: 1I49) showed striking similarity in overall shape, despite lack of sequence homology (Fig. 1d).

We aligned the SdeA CTD crystal structure with the SdeC cryo-EM map to generate a hybrid model of the full-length SidE effector (Fig. 1e). Comparison with AlphaFold3 models further highlighted CTD flexibility relative to the catalytic core (Ext. Fig. 3c, d). Notably, the N-terminal helix of the SdeA CTD crystal structure aligns with the terminal helix of the previously solved PDE-mART-CC region (PDB: 5yim), allowing seamless integration of both crystal structures. This composite model closely matches our cryo-EM/crystallographic hybrid (Ext. Fig. 3e), providing a structural framework for understanding domain organization within SidE proteins and offering the first view of CTD positioning relative to the enzymatic core.

CTD is Essential for Membrane Localization of SidE Effectors

The crystal structure of the SdeA CTD, with its resemblance to BAR domains, suggested a role in membrane association. To test this, we examined the localization of full-length EGFP-tagged SdeA, SdeB, and SdeC in HeLa cells using immunofluorescence microscopy and calnexin as an ER marker. All three effectors localized to the ER membrane (Fig. 2a). Deletion of the CTD resulted in cytosolic distribution, indicating loss of membrane targeting (Fig. 2b). Conversely, expression of the CTDs alone was sufficient to target EGFP to ER membranes in Cos7 cells (Fig. 2c), implicating the CTD as the primary membrane-targeting module.

To assess how localization influences activity, we tested whether C-terminal deletions affected the ability of SdeA to PR-ubiquitinate Rab33b, a known substrate[19,25]. In HEK293T cells, deletion constructs failed to modify Rab33b despite retaining the ability to ADP-ribosylate ubiquitin, indicating a specific loss of substrate modification (Fig. 2d). In contrast, *in vitro* assays using purified proteins showed that all but the SdeA$^{1–907}$ construct (lacking the coiled-coil region) retained Rab33b modification activity (Fig. 2e). The coiled-coil segment has been previously reported to stabilize the mART domain for catalytic activity[9,21,22]. These results suggest that membrane recruitment via the CTD is critical for efficient substrate PR-ubiquitination in a cellular context.

Identification of a Membrane-Binding motif in SidE family members

To delineate the membrane-binding interface of the SdeA CTD, we analyzed its electrostatic surface and identified three positively charged regions, which we named Mag10 (10 basic residues at the concave face), Red8 (8 residues at the C-terminal lobe), and Black4 (4 residues at the N-terminal lobe) (Fig. 3a–c). Charge-inversion mutants were generated by substituting lysine/arginine residues with glutamates. Subclassification of Mag10 into Mag5 and Mag5′, and Red8 into Red4, enabled refined mapping. All GFP-tagged mutants were expressed in Cos7 cells and analyzed for ER colocalization. While wild-type CTD and Mag10, Mag5, and Black4 mutants localized to the ER, both Red4 and Red8 mutants exhibited diffuse cytoplasmic and nuclear distribution, similar to ΔCTD constructs (Fig. 3d), identifying Red4 patch as a critical membrane-targeting segment.

Close inspection at the Alphafold3 predictions of SdeA CTD found a disordered region of the CTD within the Red4 site, that was predicted to be helical in the top-scoring predictions (Ext. Fig. 4a,b). This segment showed high b-factor values in the CTD crystal structure suggesting high conformational flexibility in this region (Ext. Fig. 4c). We generated Alphafold3 predictions[24] of the CTDs of SdeA, SdeB, SdeC and SidE to find a general resemblance of SdeA CTD crystal structure with the other family members (Ext. Fig. 4d-g). Helical wheel analysis with the help of Heliquest[26] predicted these helices to be amphipathic, a feature reminiscent of N-BAR domains such as Arfaptin, where an N-terminal amphipathic helix anchors the protein to membrane[27–29]. We hypothesized that SidE CTD might anchor the effectors in a similar fashion to the membrane. Consistently, introduction of hydrophobic-to-glutamate substitutions in these helices rendered SdeA, SdeB, and SdeC CTDs cytoplasmic and nuclear (Fig. 3e). CD spectroscopy confirmed that peptides from SdeA and SidE adopt helical conformations in the presence of liposomes[30], while peptides from SdeB and SdeC could not be tested due to insolubility (Ext. Fig. 4h, i). These results support a model in which an amphipathic helix at the distal CTD mediates membrane anchoring.

Lipid Binding Profile of SdeA CTD

Many *Legionella* effectors bind phosphoinositides such as PI3P or PI4P[31,32]. These phospholipids can interact with the electropositive patches on the proteins. To examine the lipid preference of SdeA CTD, we performed liposome interaction profiling using a microfluidic liposome microarray-based assay (LiMA)[33]. Recombinant EGFP-tagged SdeA CTD was incubated with Atto647-labeled liposomes of various compositions, and normalized binding intensities (NBI) were quantified via automated microscopy (Fig. 3f).

Wild-type SdeA CTD showed robust binding to phosphoinositide-containing liposomes, including PI4P and PI4,5P2, particularly in the context of fluidic DOPC backgrounds (Fig. 3g–h). The presence of phosphatidylserine (PS) further enhanced binding to PIP2-containing membranes (Fig. 3i–j). In contrast, the Red4 mutant failed to bind liposomes, consistent with cell-based observations (Fig. 3k). These findings were corroborated by molecular dynamics (MD) simulations: the CTD did not associate with pure POPC bilayers, but readily bound PIP-doped membranes (Ext. Fig. 5a, b). Quantification of lipid contacts revealed that PIP2 and PIP3 were enriched near basic residues of the amphipathic helix, consistent with the effects of Red4 mutations (Ext. Fig. 5c–f).

Together, these data establish that the SidE CTD harbors a functionally conserved amphipathic helix that, together with a basic surface patch, mediates specific membrane tethering through recognition of negatively charged phospholipids.

Membrane Localization Determines Substrate Specificity of SidE Effectors

We previously developed a DupA trapping strategy to identify substrates of PR-ubiquitination by catalytically inactive DupA/B mutants, which bind but do not cleave PR-Ub chains[34,35]. To test whether CTD-dependent localization governs substrate engagement, we compared full-length SdeA to either ΔCTD or Red4 mutants. Catalytically inactive (EE/AA) versions were used as controls. Immunofluorescence confirmed that while full-length SdeA and its inactive form localized to the ER, ΔCTD and Red4 mutants were cytoplasmic/nuclear (Fig. 4a). Following expression in HEK293T cells, PR-ubiquitinated substrates were captured using DupA trap and released with wild-type DupA. Quantitative mass spectrometry revealed distinct substrate profiles between wild-type and mutant constructs (Fig. 4b–c). While wild-type SdeA modified known targets like SQSTM1/p62, GORASP2, RTN1/3, STX16/17, and LNP, the ΔCTD and Red4 mutants ubiquitinated unrelated proteins (e.g., IMPDH1/2, GSTM2, HSPE1, ATP5J). These data underscore the CTD's essential role in conferring substrate specificity via localization.

We extended this analysis to full-length SdeA, SdeB, and SdeC. Upon overexpression, each effector modified hundreds of substrates, with 600 shared across all three and unique subsets: 129 (SdeA), 93 (SdeB), and 156 (SdeC) (Fig. 4d). Filtering against infection-relevant dataset[34]

narrowed this to 121 (SdeA), 113 (SdeB), and 112 (SdeC) substrates (Fig. 4e). Subcellular localization annotations from the Human Protein Atlas revealed that substrates are distributed across diverse organelles, including ER, Golgi, and mitochondria (Fig. 4f). This is consistent with the broad lipid-binding preference of SidE CTDs (see Fig. 3), indicating that substrate specificity is driven by generalized membrane targeting rather than strict organelle selectivity.

The SidE CTD Functions as a Type IV Secretion Signal

The CTD of SdeA has been previously suggested to act as a secretion signal for the Type IV secretion system (T4SS) via interaction with IcmS-IcmW-DotLc (IcmS-W-DotLc) secretion chaperone on the cytoplasmic end of the ejection site[22,36–39]. We wanted to explore the dual nature of CTDs in secretion besides their localization activity in host cells. We generated a complex of SdeA CTD with IcmS-W-DotLc subcomplex with the help of purified proteins and size exclusion chromatography (Fig. 5a-b). Initially, we had set up crystallization plates with this complex but the resulting crystals did not diffract better than 6.5 Å in our hands. Therefore, we turned to SAXS (Small angle X-ray scattering) to understand the assembly of this complex in solution[40,41].

The effective molecular masses (MMs) of the solutes are about 42 kDa, 40 kDa, and 90 kDa for IcmS-W-DotLc, SdeACTD, and SdeACTD-IcmS-W-DotLc, respectively. From the Multi-Angle Light Scattering (MALS) we observed only one significant component of the SdeACTD-IcmS-W-DotLc complex in the elusion profile with MM about 83 kDa agreeing within the credibility interval of SEC-SAXS, and the monodispersity of this complex was also confirmed as shown in Fig. 5c. This points to a quartenary complex containing one molecule of each protein. The processed SEC-SAXS data from the IcmS-W-DotLc, SdeA CTD and SdeA CTD-IcmS-W-DotLc complex are presented (black dots) in Fig. 5d. The radii of gyration R_g of the solutes for the three samples are 2.74±0.05 nm, 3.76±0.05 nm, and 3.86±0.05 nm, respectively, as calculated from the Guinier approximations in Fig. 5e. Note that in all cases, Guinier regions are linear evidencing the monodispersity of the solutes. The distance distribution functions p(r) in Fig. 5f reveal the maximum particle sizes 10±1 nm, 16±1 nm, and 15±1 nm, respectively, and indicate defined structures with limited flexibility. These properties are also confirmed by the Kratky plots (Fig. 5g). Moreover, both IcmS-W-DotLc subcomplex and SdeA CTD-IcmS-W-DotLc complex display bell-shaped p(r), indicating globular shapes. The p(r) function for SdeA CTD has a skewed appearance pointing to an elongated shape. These results suggest that IcmS-W-DotLc is bound to the central part of SdeA CTD, forming a stable globular complex.

The low-resolution shapes of the proteins and the complex were first characterized by ab initio modeling (bead models in Fig. 5h-), and Alphafold3 models were also constructed and screened against the SAXS data. Individual atomic models of IcmS-W-DotLc and SdeA CTD

fit into the SAXS envelopes quite well, whereby IcmS-W-DotLc matches into a C-shaped envelope while SdeA CTD represents a banana shaped elongated particle. A model of the SdeA CTD-IcmS-W-DotLc complex further built by rigid body analysis with SASREF fits the data with discrepancy χ^2 = 5.8. To refine this model, we performed normal mode analysis (NMA) using SREFLEX. The NMA-refined model (in Fig. 5j) has an RMSD of 6.9 Å with respect to the rigid body model and provides a further improved fit to the experimental data with χ^2 = 1.5 (Fig. 5d). This model indicates the binding of the IcmS-W-DotLc chaperone on the N-terminal side of the concave surface of SdeA CTD formed by helices α1, α2 and α3. We also compared the SAXS model of the complex with Alphafold3 prediction (Fig. 5k). The comparison showed some variation in the CTD of SdeA between the SAXS model and Alphafold3 prediction, but, importantly, the binding position of the secretion chaperone was the same in both models, lending further confidence in the obtained results.

Dual roles of SidE CTD in Membrane Binding and Secretion during Infection

Since we had generated mutants of SdeA CTD, which also included the binding site of SAXS-derived experimental model as well as Alphafold3 prediction, we performed pull-down experiments with GFP-tagged SdeA/ SdeC CTD or mutants and His-tagged IcmS-W-DotLc complex (Fig. 6a). For the wt SdeA CTD or SdeC CTD proteins, we could observe the complex formation as well as for the Mag5, Red8, and Red4 mutants. However, the Mag10 mutant did not pull-down the IcmS-W-DotLc complex. Interestingly, the Mag10 mutant corresponds to the entire concave surface of SdeA CTD, and the Mag5 mutant, which still binds to the secretion chaperone, is a subset of Mag10, belonging to the C-terminal half of the CTD. This suggested that the remaining 5 mutations of Mag10, which we termed Mag5', are responsible for binding loss. We decided to test both secretion deficient and membrane binding deficient mutants in *Legionella* infection set up.

We complemented the ΔSidE *Legionella* strain either with Flag-tagged wt SdeA or the membrane binding deficient Red4 mutant, or the secretion deficient Mag10 and Mag5 mutants. All strains expressed the complemented effectors equally upon IPTG induction as observed by the anti-Flag antibody or the GFP tag present on the proteins (Fig. 6b). The bacterial metabolic protein Isocitrate dehydrogenase (ICDH) was used as loading control[42]. To check the secretion efficiency of the mutant effectors, we separated the bacteria-infected mammalian cells with 0.2 % saponin, which only lyses the mammalian cells and leaves the bacteria intact. We probed these lysates for our flag-tagged effectors, and consistent with our previous experiments, only wt and Red4 mutant got secreted into the host whereas Mag10 and Mag5' mutant stayed in the bacteria (Fig. 6c). We also tested the above-mentioned bacterial strains for their colocalization with ER-marker in bone marrow-derived macrophages

(BMDMs) (Fig. 6d). As expected, the ΔSidE strain as well as the secretion-deficient Mag10 and Mag5' strains, did not show any immunofluorescence for the effectors. The wt SdeA complemented strain formed puncta in BMDMs, some of which colocalized with calnexin, reaffirming its ER localization in bacterial-infected cells. By contrast, the Red4 strain showed diffused distribution and no colocalization with calnexin. This confirms our understanding of the CTD in membrane binding and secretion. We further checked the effect of these mutations on the growth curve of *Legionella* in the natural host *Dictyostelium discoideum* (Fig. 6e). The indicated bacterial strains were used to infect *D. discoideum,* and the intracellular bacterial load was monitored at 2 hr, 24 hr, 48 hr, and 72 hr post-infection. The wt Lp02 strain complemented with an empty vector showed the best growth rate. The T4SS deletion strain Lp03 showed a growth defect, given that it lacks secretion of all effectors from *Legionella*. The ΔSidE strain had a growth defect when compared to the wt strain. To our surprise, this growth defect is similar in the Red4, Mag10, and Mag5' strains, suggesting that any anomaly in the CTD of SidE effectors is as drastic as the catalytic dead version of these effectors. These experiments underscore the importance of CTD in SidE activity and *Legionella* infection and establish their dual role for both secretion and membrane localization to be critical for intracellular *Legionella* replication.

Discussion

SidE family effectors represent a unique class of bacterial enzymes that co-opt the host ubiquitin system via a non-canonical phosphoribosyl-linked ubiquitination mechanism. While the enzymatic functions of their DUB, PDE, and mART domains have been well characterized, the role of the extended C-terminal domain (CTD) has remained elusive. Here, we provide structural and functional insights into this domain, revealing it as a bifunctional module critical for both membrane localization and effector translocation via the Type IV secretion system (T4SS). We also present the first cryo-EM reconstruction of full-length SdeC and the first crystal structure of SdeA CTD, providing the first integrative model of a complete SidE family effector.

Our structural model reveals that the CTD adopts a curved, banana-shaped structure and features a distal amphipathic helix embedded in a positively charged surface, allowing it to anchor to negatively charged lipid membranes, which is a hallmark of N-BAR domains[23,43]. However, unlike dimeric BAR domains, which possess two amphipathic helices enabling membrane curvature induction, SdeA CTD harbors a single membrane-anchoring helix and lacks curvature-inducing activity, as confirmed by negative-stain EM (data not shown). While structurally reminiscent of BAR domains, the CTD lacks detectable sequence homology in profile-based searches, suggesting convergent evolution of coiled-coil membrane-binding

architecture. Interestingly, a related example is BpdA from *Shewanella oneidensis*, a prokaryotic protein shown to remodel membranes via BAR-like behavior[44].

Functionally, the CTD is indispensable for effector localization to ER, Golgi, mitochondria, and vesicular membranes, sites relevant for *Legionella* replication. We extend prior work showing that PR-ubiquitination of membrane-associated substrates facilitates organelle fragmentation and membrane recruitment to Legionella-containing vacuoles (LCVs)[45,46]. Moreover, CTD-mediated anchoring to LCVs enables SidE enzymes to modify ubiquitin chains via phosphoribosylation, a process recently shown to block autophagy adaptor recruitment (e.g., p62) and suppress xenophagy[47,48].

The dual function of the CTD reflects selective pressures within both bacterial and host environments (Fig. 6f). Inside *Legionella*, the CTD serves as a secretion signal by engaging the IcmS-IcmW-DotLc chaperone complex for T4SS translocation. Once inside the host, the same domain functions as a membrane tether, localizing the effector to substrates required for effective PR-ubiquitination and intracellular replication. Disrupting either function, secretion or localization, results in phenotypes indistinguishable from SidE deletion, emphasizing the essential role of the CTD.

In conclusion, our work completes the functional annotation of the SidE effector family, positioning the CTD as a central hub that integrates effector secretion and subcellular localization. These two spatial determinants converge to control substrate selection and pathogenic function of *Legionella*. Given the prevalence of multi-domain architectures in bacterial effectors, similar dual-function localization/secretion modules may represent a broader paradigm in host-pathogen interactions.

Tables:

Table1: Cryo-EM & model data statistics

Table 2: Data collection & statistics for SdeA CTD crystal structure

Table 3: SAXS experiment, analysis and results

Table 1 – Cryo-EM and model data statistics.

	Legionella effector SdeC	
	PDE-mART domain (local refine) (EMD-50408; PDB 9FGJ)	Whole protein (3DFlex refine) (EMD-50413; PDB 9FGM)
Data collection and processing		
Magnification	130,000	
Voltage (kV)	300	
Electron dose (e^{-}/Å^2)	35	
Defocus range (μm)	−1.5 to −2.5	
Pixel size (Å)	1.077	
Symmetry imposed	*C*1	
Initial particle images (no.)	1,489,769	
Final particle images (no.)	149,162	
Map resolution (Å)	3.8	4.0
FSC threshold	0.143	0.143
Map resolution range (Å)	3.1–7.8	3.2–8.0
Refinement		
Initial model used	Model predicted using AlphaFold	PDB 9FGJ & AlphaFold model
Model resolution (Å)	4.0	3.9
FSC threshold	0.5	0.5
Model resolution range (Å)		
Map sharpening *B* factor (Å^2)	−120	−40
Model composition		
Non-hydrogen atoms	7,021	9,032
Protein residues	885	1,135
Ligands	–	–
Average *B* factors (Å^2)		
Protein	130.22	160.55
Ligand	–	–
R.m.s. deviations		
Bond lengths (Å)	0.003	0.003
Bond angles (°)	0.647	0.639
Validation		
MolProbity score	1.48	1.44
Clashscore	7.25	7.12
Poor rotamers (%)	0.0	0.0
Ramachandran plot		
Favored (%)	97.6	97.8
Allowed (%)	2.4	2.2
Disallowed (%)	0.0	0.0

401

402 **Table 2: Data collection and refinement statistics for SdeACTD crystal structure**

Legionella effector SdeA CTD		
	SdeA CTD (SAD data)	**SdeA CTD (native data, PDB code:)**
Data collection		
Beamline	SLS PX	Petra III, P14
Wavelength (Å)	1.00768	0.9763
Space group	H32	H32
Cell dimensions		
a, b, c (Å)	111.04, 111.04, 218.20	110.96, 110.96, 218.71
a, b, γ (°)	90, 90, 120	90, 90, 120
Observed reflections	740,952 (77,432)	965,988 (14,171)
Unique reflections	18,252 (2,052)	97,198 (3,992)
Resolution (Å)	47.45- 2.5	87.97-1.98
R_{merge}	0.171 (3.615)	0.062 (3.722)
R_{meas}	0.175 (3.711)	0.065 (3.908)
I/ σ(I)	17.8 (1.4)	23.9 (1.1)
$CC_{1/2}$	1.0 (0.714)	1.0 (0.586)
Completeness (%)	100 (100)	100 (100)
Redundancy	40.6 (37.7)	9.9 (3.5)
Wilson B ($Å^2$)	59.9	48.8
Phasing		
Method	SAD	MR
Resolution (Å)	2.5	
Anom. Completeness (%)	100 (100)	
Anom. multiplicity	21.1 (19.3)	
<FOM>	0.8973	
Refinement		
Copies/ a.s.u.		1/ a.s.u.
Resolution (Å)		1.98
No. reflections		36,321
R_{work}/ R_{free} (%)		21.1/ 24.3
No. atoms		2656
Protein		2576
Ligand		16
Water		64
B factors ($Å^2$)		71.15
Protein ($Å^2$)		71.28
Ligand ($Å^2$)		74.46
Water ($Å^2$)		65.28
R.m.s.d		
Bond lengths (Å)		0.011
Bond angles (°)		1.05
Ramachandran (favored/ allowed/ outlier) (%)		96.52/2.85/0.63
Clashscore		2.47
Rotamer outliers (%)		5.42

The dataset was collected from a single crystal. Values in parentheses are for highest-resolution shell. a.s.u., asymmetric unit. R.m.s.d., root mean square deviations.

Table 3: SAXS experiment, analysis and results

	IcmS-IcmW-DotLc	SdeA CTD	SdeACTD-IcmS-IcmW-DotLc
SASBDB accession code	SASDUW5	SASDUX5	SASDUY5
Data collection			
Instrument	EMBL P12 BioSAXS beamline, Petra-3, DESY, Hamburg		
Beam size at sample (µm)	200x120		
Wavelength (nm)	0.124		
s range (nm^{-1})	0.03-7.0		
Detector	Pilatus 6M		
Detector distance (m)	3		
Exposure (s per image)	1		
Column	Superdex 75 Increase 10/300 GL		
Flow rate (ml/min)	0.7		
Sample volume (µl)	100		
Sample concentration (mg/ml)	10	16.5	9
Temperature (K)	293		
Structural parameters			
R_g (nm), Guinier plot	2.74±0.05	3.76±0.05	3.86±0.05
R_g (nm), p(r) function	2.79±0.10	3.99±0.05	3.94±0.05
D_{max} (nm)	10±1	16±1	15±1
Molecular mass determination			
Theoretical MM (kDa)	45	41	86
MALLS MM (kDa)	-	-	83
SAXS MM (kDa)	42	40	90
Discrepancy of fits, χ^2			
Ab initio modelling	1.1	1.2	1.1
AlphaFold3 models	6.9	10.4	10.7
Rigid body modeling	5.9	2.6	5.8
Normal modes refinement	1.1	1.3	1.5
Data analysis software			
Data reduction	PRIMUS		
SEC-SAXS analysis	CHROMIXS		
Ab initio modelling	DAMMIF		
Homology modelling	AlphaFold3		
Computation of model scattering	CRYSOL		
Rigid body modeling	SASREF		
Normal modes refinement	SREFLEX		

Online content

Methods

Cloning and constructs

Full-length SdeA and SdeC constructs were cloned into pGEX6P1 vector using BamHI and XhoI restriction sites. SdeA CTD (1158-1499) construct was cloned into pET15b vector with NdeI and BamHI restriction sites. Full-length SdeA and SdeC were cloned into pEGFP-C1 vector using XhoI and BamHI restriction enzymes whereas for SdeB, SacI and SmaI restriction sites were used. The ΔCTD constructs were generated by mutating the V1157 to stop codon for SdeA whereas for SdeB and SdeC V1189 was mutated to a stop codon. The C-terminal domain constructs of SdeA (1158-1499) and SdeC (1190-1920) constructs were cloned into pEGFP-C1 vector using the XhoI/ BamHI sites and for SdeB (1189-1920), SacI and SmaI restriction sites were used. All the mutants were generated using site directed mutagenesis on either the full-length constructs or the C-terminal domain constructs. The EGFP-SdeA CTD construct was amplified from the pEGFP-C1 vector and cloned into pET15b vector using NdeI and BamHI sites for bacterial protein purification. C-terminal deletion constructs of SdeA were amplified from full-length SdeA cDNA and digested with BamHI and XhoI. The digested DNA fragments were inserted into pEGFP-C1 vectors digested with BamHI and XhoI. For protein expression in *E. coli*, SdeA was amplified from SdeA cDNA and digested with BamHI and XhoI. The digested DNA fragments were inserted into pGEX-6P-1 vector digested with BamHI and XhoI. We received the IcmS and IcmW genes cloned into pRSF-Duet1 vector and DotLc fragment cloned into pET22b vector from Yue Feng[22].

To generate *Legionella* strains, either full-length SdeA or the mutants were amplified with BamHI and SalI restriction sites and cloned into pZL507 vector. All the clones were confirmed by sanger sequencing. For cloning and plasmid amplifications NEB Turbo Competent *E. coli* cells were grown on LB agar plates or in LB broth.

Protein expression and purification

Proteins were expressed in the *E.coli* NEB T7 Xpress cells. Cells were grown in TB medium at 37°C until the OD reaches 0.6-0.8, induced with 0.1-0.4 mM IPTG (isopropyl β-D-l-thiogalactopyranoside), grown overnight at 25°C and collected. The cell pellet was resuspended with buffer containing 50mM Tris-HCL, 0.5 M NaCl, 25 mM Imidazole, 5% glycerol, pH 7.5 and lysed by high pressure cell disruptor. Cell debris were removed by centrifugation at 14,000x g for one hour, supernatant was collected, applied to either His-tag affinity purification or GST-tag affinity purification. His-tagged proteins were eluted with 250 mM imidazole in the lysis buffer whereas GST tagged proteins were eluted with 15 mM glutathione freshly added to the binding buffer. His-tag from the His-SdeA-CTD construct in

pET15b vector was cleaved using Thrombin protease. For proteins required for structural and biophysical studies (like SdeC FL, SdeA CTD and IcmS-IcmW-DotLc), two more steps of purification were carried out in the form of anion exchange chromatography (Hiprep Q HP) and then size exclusion chromatography. All proteins were stored in the buffer 25 mM Tris-HCl, 200 mM NaCl, pH 7.5; 1 mM TCEP. IcmS-IcmW-DotLc subcomplex was purified by mixing the pellets obtained from IcmS-IcmW expression from pRSF-Duet1 vector and DotLc expression from pET22b vector as described before[22].

Cryo-EM grid preparation and data collection

EM sample preparation and data collection were carried out at the EM facility of MPI, Biophysics. 3 µL of protein at a concentration of about 0.3 mg/ml was applied to a 300-mesh gold Quantifoil® R 2/2 grid with gold support. The grid was blotted with Whatman® No. 1 filter paper and plunged into liquid ethane cooled to liquid nitrogen temperature. Imaging was performed on a Thermo Fisher Titan Krios operated at 300 kV equipped with a Gatan K2 Summit® direct electron detector and a Gatan Quantum® energy filter. Movies containing 40 frames were collected at 130,000x magnification in counting mode with a physical pixel size of 1.077 Å, total dose on all frames were 33 e-/.2. Defocus values of the images ranged from -1.5 to - 2.5 µm. Two rounds of datasets were collected by the automated imaging software EPU.

Cryo-EM image processing

Both cryo-EM datasets were processed following the same method: The original movies were first subjected to beam-induced motion correction and dose-weighting using MotionCor2, and the contrast transfer function (CTF) parameters were determined using CTFFIND4[49,50]. Images with estimated poor resolution (> 5.5 Å) and severe astigmatism (> 550 Å) were removed at this step. Particles were picked by TOPAZ[51] and used for all further processing step. 2D classification, initial model generation, 3D classification, CTF refinement, and Bayesian polishing were performed using RELION 4.0[52,53]. The polished particles generated from RELION were subjected to cryoSPARC for heterogeneous refinement, non-uniform refinement, and 3DFlex refinement[54,55]. A schematic overview of the data processing workflow, and a summary of map qualities are shown in Extended Fig. 1 and Table 1.

Model building and geometry refinement

The sub-atomic model of SdeC was built into the cryo-EM map using ChimeraX[56] with ISOLDE[57] add-in and COOT[58], based on the AlphaFold predicted structure as an initial template[24]. The PDE-mART domain was built into the local refinement map of SdeC. The CC

and CTD were built into the 3DFlex backbone tracing and docking of side chains[59]. Refinement results were manually inspected and corrected if required. The model quality was validated by MolProbity[60] of the PHENIX package. Map-to-model cross-validation was performed in PHENIX[60]. A summary of model parameters and the corresponding cryo-EM map statistics is found in Table 1. Visualization of the cryo-EM maps and model was done in ChimeraX and Pymol (The PyMOL Molecular Graphic System, Version 3.0 Schrödinger, LLC).

Crystallization

The tag-free SdeA CTD protein was concentrated to 10 mg/ml and was screened with sitting drop matrix screens in 96-well plate with 300 nL of protein and 300 nL of precipitant solution at 293K with a mosquito crystallization robot (TTP Labtech). Diffraction quality crystal appeared from solution containing 0.2 M sodium chloride, 0.1 M sodium/ potassium phosphate pH-7.5 and 50% PEG 200. For SAD-phasing, the crystals were soaked in ethyl mercury thiosalisylate (EMTS). Crystals were cryo-protected using mother liquor solution supplemented with 25% (v/v) ethylene glycol before flash-freezing into liquid nitrogen.

Data collection, processing and structure determination

Diffraction data were collected on single frozen crystal in a nitrogen stream at 100K at beamline P14 at Petra III, DESY, Hamburg. The diffraction data were integrated with the program XDS[61] and scaled with AIMLESS[62], which is part of the CCP4 package[63] and the resolution was estimated to be around 2 Å. However, due to unavailability of closely related structures we were not able to find phases for structure solution. To determine the phases, we soaked the native crystals in EMTS to use mercury as heavy atom for anamolous scattering[64]. We collected diffraction data from these crystals at PXI beamline in SLS, Villigen at 1.00768 Å wavelength. With the help of AutoSol[65] and AutoBuild[66] programs of Phenix, we could identify 5 mercury binding sites, which could help solve the phase problem and build model into the 2 Å native crystallographic dataset. Structure refinement and manual model building were performed with Coot[58] and Phenix.refine[67]. Validation of the final models was performed using MolProbity[60]. The resulting model was visualized with Pymol (The PyMOL Molecular Graphic System, Version 3.0 Schrödinger, LLC).

***Legionella* strains**

L. pneumophila strains used in this study were derivatives of the Philadelphia 1 strain Lp02 ΔsidE strain as described and were grown and maintained on CYE medium or in AYE broth. Lp03 is an isogenic *dotA*$^-$ mutant. When necessary antibiotics were included. For complementation experiments, the genes were inserted into pZL507. All infections were performed with bacterial cultures grown to the post-exponential phase as judged by optical

density of the cultures (OD600 = 3.5–3.8) as well as increase of bacterial motility. The integrity of all constructs was verified by sequencing analysis.

Cell culture and infection

HeLa, HEK293T and A549 cells were cultured in high glucose Dulbecco's Modified Eagles Medium (DMEM) supplemented with 10% fetal bovine serum (FBS), 100 U/mL penicillin and 100 mg/mL streptomycin at 37 °C, 5% CO2 in a humidified incubator. Transfection was performed using polyethyleneimine (PEI) reagent or Genejuice (Merck). Cells grown to about 80% confluence were infected with indicated *L. pneumophila* strains. *D. discoideum* strains AX4 and AX4-HDEL–GFP were cultured in HL-5 medium. 2×10^5 *D. discoideum* cells seeded in 24-well plates were infected with an MOI of 0.05 for growth experiments[68]. In all cases, 1.5 hours after adding bacteria to cultured cells, infections were synchronized by washing the infected cells three times with warm PBS buffer. Total bacterial counts at indicated time points were determined by plating serially diluted saponin lysates onto bacterial media.

To determine protein translocation by *L. pneumophila*, HEK293T cells were transfected to express FCγRII for 24 h with Lipofectamine 3000 (Life Technology). Bacteria of relevant *L. pneumophila* strains were opsonized with rabbit anti-*Legionella* antibodies at 1:500 for 30 min before infecting the cells at an MOI of 20 for 2 h. Cells infected with the indicated bacterial strains were lysed with 0.2% saponin 2 hpi, which lyses membranes of mammalian cells but not of bacterial cells. The lysates were directly probed with Flag antibody.

Antibodies and reagents

All reagents were from Sigma, Roche or Roth. The following antibodies were used: antibodies against HA (C367S), GFP (sc-9996), ubiquitin (P4BD) from Cell signaling and ubiquitin (ab7254) from Abcam respectively; anti-ADPR (Millipore, MABE1016), anti-Flag (Sigma, F1804), GST (2622), Tubulin (ab6046), Calnexin (ab22595), GAPDH (D16H11) from Cell signaling. Monoclonal Anti-HA−Agarose antibody (HA-7) was purchased from Sigma. GFP trap beads were purchased from ChromoTek, gta-100 and Pro-Q diamond stain was obtained from Thermo Fischer, P33300.

Confocal imaging and image analysis

Confocal images were obtained using a Zeiss LSM780 microscope system fitted with a 63 x 1.4 NA oil-immersion objective as well as argon and helium – neon ion lasers for the excitation of GFP (488 nm) and RFP (546 nM), respectively. Images were analyzed in FIJI to determine recruitment of proteins to cellular compartments.

Immunostaining and immumobloting

For immunostaining, anti-Flag antibody was used at 1:500. Antibodies against Calnexin (ab22595, 1:100) was purchased from abcam; Cell fixation, permeabilization and immunostaining were performed as described. Briefly, cells infected with the indicated bacterial strains at an MOI of 10 were washed once with PBS, pH 7.4, and fixed with 4% paraformaldehyde (PFA) in PBS for 10 min at room temperature. Cells were washed again with PBS 3 times, then permeabilized with 0.1% saponin in PBS for 12 min, and blocked with blocking buffer containing 4% BSA in PBS for 1 h at room temperature. Cells were stained with antibodies diluted in blocking buffer overnight at 4 °C and washed with PBS three times next day. Cells were further incubated with Alexa Flour dyes-conjugated secondary antibodies for 1 h at room temperature in the dark and washed with PBS and incubated with DAPI in PBS, followed with further 2 times washing with PBS. Processed samples were inspected and scored using an Olympus IX-81 fluorescence microscope.

For immunoblotting, Cell lysates or immunoprecipitated proteins were mixed with SDS sample buffer, heated at 95 °C for 5 min, centrifuged, and separated by Tris-Glycine SDS-PAGE, and transferred to PVDF membrane (Millipore) at cold room. Blots were blocked with 5% non-fat milk for 1 h at room temperature and incubated with primary antibodies overnight at cold room or 2 h at room temperature and washed with TBST (0.1% Tween 20 in TBS) three times. The blots were further incubated with secondary antibodies for 1 h at room temperature and washed 3 times with TBST. The blots were incubated with ECL reagents (advansta), and chemiluminescence was acquired with the Bio-Rad ChemiDoc system.

For the *Legionella* infection experiments, nitrocellulose membrane was used for blotting. After blocking with 5% milk, membranes were incubated with the appropriate primary antibody: anti-Flag (Sigma, F1804), 1:2,000; anti-ICDH, 1:2,000; Tubulin (DSHB, E7), 1:10,000. Membranes were incubated with an appropriate IRDye infrared secondary antibody (Li-Cor's Biosciences Lincoln, Nebraska, USA) and the signals were obtained by using the Odyssey infrared imaging system.

PR-ubiquitination assay

SdeA-mediated PR-Serine ubiquitination *in vitro* reaction was done as previously described[21]. Briefly, 2 µg of purified Rab33b was incubated with 1 µM SdeA and 25 µM ubiquitin in the presence of 200 µM of NAD+ in 40 µL of reaction buffer (50mM NaCl and 50mM Tris, pH 7.5) for 1 h at 37 °C. The samples were analysed by SDS-PAGE and western blotting.

Simulations of protein-membrane docking

A coarse-grained (CG) model of Sde-CTD was prepared using the MARTINI force-field v2.2[77] using the *martinize.py* script[69]. Secondary structure restraints were imposed with DSSP

assignments. A POPC (16:0-18:1 PC) bilayer spanning a periodic box of $20 \times 20\ nm^2$ was constructed using insane.py[70]. The protein was initially placed at a distance of 5 nm from membrane surface and solvated with CG water containing 150 mM NaCl. For comparison, another system was generated with same configuration, but the POPC bilayer was doped with 10% PIPs (5% PIP2 and 5% PIP3). Both these systems were energy minimized using the steepest descent algorithm for 3000 steps and then equilibrated the system with position restraints on the backbone (BB) beads, first under NVT conditions (T = 310 K) and then under NPT (P = 1 bar) conditions. Five short equilibrations, with increasing time steps (dt = [1, 2, 5, 10, 20] fs), were employed following the CHARMM-GUI protocol. Subsequently, we performed production runs for 3 µs for each system using a 20 fs timestep under NPT conditions (1 bar; 310 K). The Berendsen thermostat and the Berendsen semi-isotropic barostat[71] were used for the equilibration phases and the velocity-rescale thermostat[72], while the Parinello-Rahman semi-isotropic barostat[73] was employed for the production phase, respectively. All CGMD simulations were performed using GROMACS v2020.1[74]. The total number of PIP2 and PIP3 contacts were computed as a function of time. Following that the contact frequency was estimated for each residue and the binding sites were identified using a 40% cutoff.

Normal Mode Analysis

The SdeA-CTD X-ray model was refined using Modeller[75] to model unresolved loop regions within the structure, followed by energy minimization with GROMACS[74]. 5 models were constructed using AlphaFold2 for the full-length SdeC and used for fitting into the cryoEM map. An elastic network was mapped onto the top-ranked AF2[76] model using Cα atoms (cutoff = 1 nm) first followed by computation of the 5 lowest frequency normal modes between amplitudes (DQ -100 and 100) using a step size of 20 as implemented in *bio3D-nma*[77]. Elastic network and eigen vectors corresponding to the top 3 low-frequency modes were visualized using Pymol along their residue correlations.

Liposome microarray-based assay (LiMA)

The recruitment of SdeA and Red4 to membranes was assessed with LiMA, as described previously[30]. In brief, lipid mixtures containing 10 mol% phosphatidylinositol phosphates or glycerophospholipids in a DOPC and POPC background and organellar membrane mimics were spotted on a thin agarose layer (Supplementary Table 1). Cooperativity was probed by including phosphatidylinositol phosphate spots with an additional 10 mol% PS. Pegylated PE and PE-Atto647N were added to each mixture to facilitate the formation and visualisation of the liposomes. The microarray was hydrated with buffer A (25 mM Tris pH 7.5, 200 mM NaCl, 5 mM DTT) and the self-assembly of liposomes was verified with fluorescence microscopy. The EGFP-tagged SdeA and Red4 were diluted in buffer A to 1 µM and centrifuged for 5

minutes at maximum speed in a table-top centrifuge to remove aggregates. 40 μL of the diluted protein was incubated on the microarray for 1 hour at room temperature. A positive control, the strong PI(4,5)P_2-binder PH-PLCδ, was incubated in parallel at 1 μM for 30 minutes at room temperature. Unbound protein was washed away with 80 μL buffer A. The microarray chips were imaged with automated fluorescence microscopy. Images were taken for the Atto647 (5 ms exposure time) and EGFP fluorescence (5, 10, 20, 30, 40, 50, 75, 100, 150, 200, and 300 ms exposure times). The images were processed with the pre-established CellProfiler pipeline and rLima script[30]. Only unsaturated EGFP pixels that overlapped with the Atto647 fluorescence were taken into account. The normalised binding intensity was calculated as the ratio between EGFP and Atto647 fluorescence corrected for the exposure time. Each protein-lipid spot combination was performed in triplicates.

Identification of substrates of SidE family DupA trapping mutant and mass-spec analysis

Cells were transfected with FL SdeA, SdeA ΔCTD, SdeA Red4 mutant, FL SdeB and FL SdeC or their catalytically inactive counterparts (EE/AA mutants). Following transfections, cells were lysed in SDS-lysis buffer (50 mm Tris, 2% SDS, 10 mm TCEP [Sigma 646,547], 40 mm chloroacetamide [Sigma, C0267], protease inhibitor cocktail, phosphatase inhibitor [Sigma, PHOSS-RO]) and heated to 95°C for 10 min. The lysate was incubated with resin containing GST-tagged DupA inactive mutant which specifically traps PR-ubiquitinated substrates, following wash. The eluted proteins were denatured by addition of 1 volume of 8 M urea in 50 mM Tris pH 8, cysteines were reduced and alkylated with TCEP and chloroacetamide. Proteolytic digest was performed for 3 h with 0.5 mg LysC (Wako) and after dilution to < 2 M Urea with 0.5 mg Trypsin (Promega) over night at 37 C. Tryptic peptides were desalted by Stage-Tips and analyzed on a Q Exactive HF (Thermo Fisher) coupled to an easy-LC 1200 (Thermo). In brief, peptides were separated with a non-linear 70 min gradient from 5%–35% solution B (80% Acetonitrile, 0.1% formic acid) on a 20 cm column packed with 1.9 mm C18 material (Dr. Maisch) and injected online into the mass-spectrometer. Survey scans were recorded with a resolution of 60,000 and the 15 most abundant precursor ions were subjected to HCD fragmentation. Data analysis was performed with MaxQuant 1.6.11 against the uniport human reference proteome database (December 2017). Label-free quantification was performed by MaxLFQ quantification with activated match-between-runs. Statistical testing and GO annotation were done with Perseus (1.6.1.1). Missing values in the control samples (SdeA EE/AA, SdeB EE/AA and SdeC EE/AA mutants) were amputated and proteins, that were significantly enriched in WT samples were identified by 5% FDR corrected T-Tests. Geneontology (GO) terms that were overrepresented among the potential SidE substrates

were detected by a FDR 5% corrected test by the Panther website[78]. Missing values were imputed from normal distribution of data using default settings. Significant candidates were chosen using two-sided t test with error-corrected p-values (0.01. FDR) and log2 (fold change) value minimum of ±0.5. To avoid false-positive protein identification, ≥2 unique peptides identified within a single protein were used for further analysis. Network and gen ontology analysis was performed with statistically significant hits using the online Metascape software.

SidE proteins exclusive and common substrates analysis

We utilized proteomics data that quantified the differential abundance of substrates captured by catalytically inactive DupA and DupB in the presence of full-length or ΔCTD SidE proteins (SdeA, SdeB, and SdeC). We selected the entries that displayed significant differences in abundance, according to Student's *t*-test (-log p-value ≥1.3, between the WT SidE proteins and their inactive/mis-localized mutant). We filtered for protein entries displaying abundance ratio ≥1.0 (log units, negative ratios were discarded) and ensured that at least two or more unique peptides mapped to them. We then filtered for substrates that were also detected in the infection settings published before[34]. To display the sub-cellular localizations of the substrates, we filtered for the substrates common to SdeA, SdeB, and SdeC, found both under transfection and infection settings. The cellular localization data were retrieved, from the Human Protein Atlas[79]. We filtered for entries describing protein's presence using "supported", "approved", or "enhanced" evidence annotations. We collected both primary and secondary cellular localizations. For each cellular compartment, we obtained the sum of the protein abundance ratios for each of the three proteins SdeA, SdeB, and SdeC, respectively.

Circular Dichroism Spectroscopy

We prepared liposomes with the composition of 85% DOPC, 5% DOPS, 25% POPE and 5% Cholesterol. The liposomes were freshly extruded with a 0.2 μM cut-off filter. 0.5 mM liposomes were incubated with 100 μM of the peptides in 10 mM potassium phosphate buffer at pH-7.0. CD spectroscopy was carried out at 20 ^{o}C on a Jasco J-810 spectropolarimeter. Three measurements were obtained for each sample between the wavelengths 190-260 nM at a speed of 30 nm/ min. Readings above 600 V were excluded. The mean of the triplates was plotted to obtain the secondary structure profile of the peptides either in the presence or absence of liposomes[30].

SEC–MALS

SEC–MALS measurements were performed on an Agilent Infinity II high-performance liquid chromatography (HPLC) system coupled to a Wyatt DAWN NEON 8 angle detector, an Optilab online refractive index detector and an Agilent VWD ultraviolet detector. Protein solutions (60

µl at 2 mg ml−1) were injected and separated on a Superdex 75 Increase 10/300 column (Cytiva) with a flow of 0.5 ml min−1 in 20 mM Tris pH 8.0 and 100 mM NaCl. Masses were determined with the program Astra (Wyatt Technology) using BSA for calibration.

Small- Angle X-ray Scattering (SAXS)

The samples of IcmS/IcmW/DotLc, SdeACTD and SdeACTD-IcmSWDotLc complex at concentrations of 10 mg/ml, 16.5 mg/ml, and 9 mg/ml, respectively, were measured at the EMBL P12 beamline of PETRA III – DESY (Hamburg, Germany)[80]. SEC coupled to SAXS measurements (SEC-SAXS) were conducted using the X-ray wavelength of λ = 0.124 nm with the Pilatus 6 M detector positioned at 3 m from the sample. The covered range of the scattering vector was 0.03 nm^{-1} < s < 7.0 nm^{-1} with $s=4\pi sin\theta/\lambda$, where 2θ is the scattering angle. The SEC-SAXS measurements of IcmS/IcmW/DotLc, SdeACTD and their complex were performed using an Agilent 1260 Infinity II Bio-inert LC system and analytical columns Superdex 75 increase 10/300 GL, Superdex 75 increase 10/300 GL, Superdex 75 increase 10/300 GL, respectively, equilibrated with the samples buffer (25 mM Tris-HCl, 200 mM NaCl pH 7.5, 5 mM DTT). In parallel to the SEC-SAXS, MALS measurements were conducted. Protein elution was detected by absorbance at 280 nm. The samples and buffers were stored at -80℃ prior to the experiments and measured at 20 ºC.

The injection volume was 100 μl, and the flow rate was 0.7 mg/ml. For each sample, 2100 exposures, each lasting 1 sec, were collected, and checked for radiation damage using the SASFLOW pipeline[80]. The samples and buffer subtractions were handled by Chromixs[81]. The data was analyzed using the programs from the ATSAS package[82]. The radius of gyration R_g was determined using the Guinier approximation[83]. The particle distance distribution functions p(r) were computed by GNOM[84] and the *ab initio* shapes were restored using DAMMIN[85]. The scattering from atomic models was computed by CRYSOL[86].

In vitro pull-down assay: GFP-SdeA-CTD-pET15b for pull-downs

With the help of GFP-trap beads we immobilized GFP-tagged SdeA CTD protein and the mutants on the beads. The same amount of His-tagged IcmS-IcmW-DotLc complex was incubated for two hours with SdeA-coated beads at 4 °C. Following incubation, the beads were washed with binding buffer and the samples were boiled at 95 °C for 5 minutes and applied to SDS-PAGE. The gel was stained using silver staining protocol (Thermo Scientific; 24612).

Data and code availability

The atomic models of crystal structures and cryo-EM coordinates reported in this paper have been deposited in the Protein Data Bank (PDB codes: 9FGJ; 9FGM,). The cryo-EM maps

have been deposited to EMDB (EMD-50408; EMD-50413). The SAXS data and models have been deposited in the SASBDB (SASDUW5; SASDUX5; SASDUY5).
Mass spectrometric data pertaining to PR-ubiquitination of substrates upon overexpression of SdeA FL, SdeA ΔCTD, SdeA-Red4 mutant, SdeB and SdeC available upon request.

Acknowledgements

The cryo-EM datasets were collected at the MPI Biophysics EM facility. The X-ray diffraction was collected at the Swiss Light Source PX beamline and P14 Petra III (DESY, Hamburg, Germany). We thank the scientific staff at SLS PX and Petra III P14 beamlines for their support. IcmS, IcmW, and DotLc constructs were kindly provided by Yue Feng. We thank the staff at the quantitative proteomics Unit of IBC2 for using their proteomics platform and the Frankfurt Center for Advanced Microscopy (FCAM) for access to microscopes. We thank Volker Dötsch for access to the CD spectroscopy and Anshu Khatri for help with the measurements. We also thank L. Arvind (NCBI/NLM/NIH) for valuable comments and discussions. R.M.B. and G.H. thank the Center for Supercomputing, GUF (Goethe-HLR cluster), and the Max-Planck Computing and Data Facility (MPCDF clusters) for computing time. A.C.G. and L.E. acknowledge the financial support of the Louis-Jeantet Foundation and the Swiss National Science Foundation (grant 320030-227988). This work was supported by the DFG-funded Collaborative Research Center on Selective Autophagy (SFB1177) Project-ID 253130777 and by the EUbOPEN Innovative Medicines Initiative 2 Joint Undertaking (JU) under grant agreement No. 875510.

Author Contributions

M.M. and I.D. conceived the project. M.M. designed constructs, protein purification, biochemistry, performed crystallization, structure solution, model building and refinements. W.C., M.M., M.K., collected the EM images and T.-H. W. and S.S. did the image processing, and model building and refinement. R.M. performed the immunofluorescence experiments. A.C., and R.M.B., performed structural modelling, MD simulations, NMA analysis, and GO analysis of MS data with technical support from G.H. A.B. performed pull-downs and mass spectrometry and A.C. helped with proteomics data analysis. L.E. and A.C.G. designed and performed the liposome microarray experiments. A.M. and D.S. performed SAXS and data analysis. Y.L. performed the PR-ubiquitination assays and A.V. helped with the biochemistry. J.P. and D.G. provided excellent technical assistance. G.H.N. provided the peptides for CD spectroscopy. C.L. and Z.-Q.L. performed bacterial infection experiments. All authors designed experiments, analysed data and interpreted results. M.M. and I.D. wrote the manuscript with input from all authors. I.D. supervised the project.

Competing financial interests

The authors declare no competing interests.

Supplementary Table 1: Liposome composition for LiMA (Excel sheet).

References

1. Isberg, R. R., O'Connor, T. J. & Heidtman, M. The Legionella pneumophila replication vacuole: making a cosy niche inside host cells. *Nat. Rev. Microbiol.* **7**, 13–24 (2009).
2. Finsel, I. & Hilbi, H. Formation of a pathogen vacuole according to Legionella pneumophila: how to kill one bird with many stones. *Cell. Microbiol.* **17**, 935–950 (2015).
3. Mondino, S. *et al.* Legionnaires' Disease: State of the Art Knowledge of Pathogenesis Mechanisms of Legionella. *Annu. Rev. Pathol.: Mech. Dis.* **15**, 1–28 (2019).
4. Tomaskovic, I., Gonzalez, A. & Dikic, I. Ubiquitin and Legionella: From bench to bedside. *Semin. Cell Dev. Biol.* **132**, 230–241 (2022).
5. Waksman, G. From conjugation to T4S systems in Gram-negative bacteria: a mechanistic biology perspective. *EMBO Rep.* **20**, EMBR201847012 (2019).
6. Schator, D. *et al.* Legionella para-effectors target chromatin and promote bacterial replication. *Nat. Commun.* **14**, 2154 (2023).
7. Black, M. H. *et al.* Bacterial pseudokinase catalyzes protein polyglutamylation to inhibit the SidE-family ubiquitin ligases. *Science* **364**, 787–792 (2019).
8. Bhogaraju, S. *et al.* Inhibition of bacterial ubiquitin ligases by SidJ–calmodulin catalysed glutamylation. *Nature* **572**, 382–386 (2019).
9. Gan, N. *et al.* Regulation of phosphoribosyl ubiquitination by a calmodulin-dependent glutamylase. *Nature* **572**, 387–391 (2019).
10. Mukherjee, R. & Dikic, I. Regulation of Host-Pathogen Interactions via the Ubiquitin System. *Annu. Rev. Microbiol.* **76**, 211–233 (2022).

11. Roberts, C. G., Franklin, T. G. & Pruneda, J. N. Ubiquitin-targeted bacterial effectors: rule breakers of the ubiquitin system. *EMBO J.* **42**, EMBJ2023114318 (2023).
12. Wasilko, D. J., Huang, Q. & Mao, Y. Insights into the ubiquitin transfer cascade catalyzed by the Legionella effector SidC. *eLife* **7**, e36154 (2018).
13. Steinbach, A. *et al.* Cross-family small GTPase ubiquitination by the intracellular pathogen Legionella pneumophila. *Mol. Biol. Cell* **35**, ar27 (2024).
14. Kubori, T., Arasaki, K., Oide, H., Kitao, T. & Nagai, H. Multi-tiered actions of Legionella effectors to modulate host Rab10 dynamics. *eLife* **12**, RP89002 (2024).
15. Schulze-Niemand, E., Naumann, M. & Stein, M. The Activation and Selectivity of the Legionella RavD Deubiquitinase. *Front. Mol. Biosci.* **8**, 770320 (2021).
16. Wan, M. *et al.* A bacterial effector deubiquitinase specifically hydrolyses linear ubiquitin chains to inhibit host inflammatory signalling. *Nat. Microbiol.* **4**, 1282–1293 (2019).
17. Shin, D. *et al.* Bacterial OTU deubiquitinases regulate substrate ubiquitination upon Legionella infection. *eLife* **9**, e58277 (2020).
18. Kang, S. *et al.* Structural insights into ubiquitin chain cleavage by Legionella ovarian tumor deubiquitinases. *Life Sci. Alliance* **6**, e202201876 (2023).
19. Qiu, J. *et al.* Ubiquitination independent of E1 and E2 enzymes by bacterial effectors. *Nature* **533**, 120–124 (2016).
20. Bhogaraju, S. *et al.* Phosphoribosylation of Ubiquitin Promotes Serine Ubiquitination and Impairs Conventional Ubiquitination. *Cell* **167**, 1636-1649.e13 (2016).
21. Kalayil, S. *et al.* Insights into catalysis and function of phosphoribosyl-linked serine ubiquitination. *Nature* **557**, 734–738 (2018).
22. Dong, Y. *et al.* Structural basis of ubiquitin modification by the Legionella effector SdeA. *Nature* **557**, 674–678 (2018).
23. Simunovic, M., Evergren, E., Callan-Jones, A. & Bassereau, P. Curving Cells Inside and Out: Roles of BAR Domain Proteins in Membrane Shaping and Its Cellular Implications. *Annu. Rev. Cell Dev. Biol.* **35**, 1–19 (2019).
24. Abramson, J. *et al.* Accurate structure prediction of biomolecular interactions with AlphaFold 3. *Nature* **630**, 493–500 (2024).

851 25. Kawabata, M. *et al.* Legionella hijacks the host Golgi-to-ER retrograde pathway for
852 the association of Legionella-containing vacuole with the ER. *PLoS Pathog.* **17**,
853 e1009437 (2021).
854 26. Gautier, R., Douguet, D., Antonny, B. & Drin, G. HELIQUEST: a web server to
855 screen sequences with specific α-helical properties. *Bioinformatics* **24**, 2101–2102
856 (2008).
857 27. Boucrot, E. *et al.* Membrane Fission Is Promoted by Insertion of Amphipathic
858 Helices and Is Restricted by Crescent BAR Domains. *Cell* **149**, 124–136 (2012).
859 28. Herlo, R. *et al.* An Amphipathic Helix Directs Cellular Membrane Curvature
860 Sensing and Function of the BAR Domain Protein PICK1. *Cell Rep.* **23**, 2056–2069
861 (2018).
862 29. Kefauver, J. M. *et al.* Cryo-EM architecture of a near-native stretch-sensitive
863 membrane microdomain. *Nature* **632**, 664–671 (2024).
864 30. Arakawa, T. *et al.* Structure Analysis of Proteins and Peptides by Difference
865 Circular Dichroism Spectroscopy. *Protein J.* **40**, 867–875 (2021).
866 31. Luo, X. *et al.* Structure of the Legionella Virulence Factor, SidC Reveals a Unique
867 PI(4)P-Specific Binding Domain Essential for Its Targeting to the Bacterial
868 Phagosome. *PLoS Pathog.* **11**, e1004965 (2015).
869 32. Pike, C. M., Boyer-Andersen, R., Kinch, L. N., Caplan, J. L. & Neunuebel, M. R.
870 The Legionella effector RavD binds phosphatidylinositol-3-phosphate and helps
871 suppress endolysosomal maturation of the Legionella-containing vacuole. *J. Biol.*
872 *Chem.* **294**, 6405–6415 (2019).
873 33. Saliba, A.-E. *et al.* A protocol for the systematic and quantitative measurement of
874 protein–lipid interactions using the liposome-microarray-based assay. *Nat. Protoc.* **11**,
875 1021–1038 (2016).
876 34. Shin, D. *et al.* Regulation of Phosphoribosyl-Linked Serine Ubiquitination by
877 Deubiquitinases DupA and DupB. *Mol. Cell* **77**, 164-179.e6 (2020).
878 35. Liu, Y. *et al.* Serine-ubiquitination regulates Golgi morphology and the secretory
879 pathway upon Legionella infection. *Cell Death Differ.* **28**, 2957–2969 (2021).
880 36. Bardill, J. P., Miller, J. L. & Vogel, J. P. IcmS-dependent translocation of SdeA into
881 macrophages by the Legionella pneumophila type IV secretion system. *Mol. Microbiol.*
882 **56**, 90–103 (2005).

883 37. Ninio, S., Zuckman-Cholon, D. M., Cambronne, E. D. & Roy, C. R. The Legionella
884 IcmS–IcmW protein complex is important for Dot/Icm-mediated protein translocation.
885 *Mol. Microbiol.* **55**, 912–926 (2005).
886 38. Cambronne, E. D. & Roy, C. R. The Legionella pneumophila IcmSW Complex
887 Interacts with Multiple Dot/Icm Effectors to Facilitate Type IV Translocation. *PLoS*
888 *Pathog.* **3**, e188 (2007).
889 39. Kwak, M.-J. *et al.* Architecture of the type IV coupling protein complex of Legionella
890 pneumophila. *Nat. Microbiol.* **2**, 17114 (2017).
891 40. Petoukhov, M. V. & Svergun, D. I. Global Rigid Body Modeling of Macromolecular
892 Complexes against Small-Angle Scattering Data. *Biophys. J.* **89**, 1237–1250 (2005).
893 41. Franke, D., Kikhney, A. G. & Svergun, D. I. Automated acquisition and analysis of
894 small angle X-ray scattering data. *Nucl. Instrum. Methods Phys. Res. Sect. A: Accel.,*
895 *Spectrometers, Detect. Assoc. Equip.* **689**, 52–59 (2012).
896 42. Xu, L. *et al.* Inhibition of Host Vacuolar H+-ATPase Activity by a Legionella
897 pneumophila Effector. *PLoS Pathog.* **6**, e1000822 (2010).
898 43. Mim, C. & Unger, V. M. Membrane curvature and its generation by BAR proteins.
899 *Trends Biochem. Sci.* **37**, 526–533 (2012).
900 44. Phillips, D. A. *et al.* A bacterial membrane sculpting protein with BAR domain-like
901 activity. *eLife* **10**, e60049 (2021).
902 45. Kim, S. & Isberg, R. R. The Sde phosphoribosyl–linked ubiquitin transferases
903 protect the Legionella pneumophila vacuole from degradation by the host. *Proc. Natl.*
904 *Acad. Sci.* **120**, e2303942120 (2023).
905 46. Kotewicz, K. M. *et al.* A Single Legionella Effector Catalyzes a Multistep
906 Ubiquitination Pathway to Rearrange Tubular Endoplasmic Reticulum for Replication.
907 *Cell Host Microbe* **21**, 169–181 (2017).
908 47. Wan, M. *et al.* Phosphoribosyl modification of poly-ubiquitin chains at the
909 Legionella-containing vacuole prohibiting autophagy adaptor recognition. *Nat.*
910 *Commun.* **15**, 7481 (2024).
911 48. Kotewicz, K. M. *et al.* Sde proteins coordinate ubiquitin utilization and
912 phosphoribosylation to establish and maintain the Legionella replication vacuole. *Nat.*
913 *Commun.* **15**, 7479 (2024).
914 49. Zheng, S. Q. *et al.* MotionCor2: anisotropic correction of beam-induced motion for
915 improved cryo-electron microscopy. *Nat. Methods* **14**, 331–332 (2017).

916 50. Rohou, A. & Grigorieff, N. CTFFIND4: Fast and accurate defocus estimation from
917 electron micrographs. *J. Struct. Biol.* **192**, 216–221 (2015).
918 51. Bepler, T. *et al.* Positive-unlabeled convolutional neural networks for particle
919 picking in cryo-electron micrographs. *Res. Comput. Mol. Biol.: Annu. Int. Conf.,*
920 *RECOMB : Proc. RECOMB (Conf. : 2005-)* **10812**, 245–247 (2018).
921 52. Scheres, S. H. W. RELION: Implementation of a Bayesian approach to cryo-EM
922 structure determination. *J. Struct. Biol.* **180**, 519–530 (2012).
923 53. Kimanius, D., Dong, L., Sharov, G., Nakane, T. & Scheres, S. H. W. New tools for
924 automated cryo-EM single-particle analysis in RELION-4.0. *Biochem. J.* **478**, 4169–
925 4185 (2021).
926 54. Punjani, A., Rubinstein, J. L., Fleet, D. J. & Brubaker, M. A. cryoSPARC: algorithms
927 for rapid unsupervised cryo-EM structure determination. *Nat. Methods* **14**, 290–296
928 (2017).
929 55. Punjani, A., Zhang, H. & Fleet, D. J. Non-uniform refinement: adaptive
930 regularization improves single-particle cryo-EM reconstruction. *Nat. Methods* **17**,
931 1214–1221 (2020).
932 56. Goddard, T. D. *et al.* UCSF ChimeraX: Meeting modern challenges in visualization
933 and analysis. *Protein Sci.* **27**, 14–25 (2018).
934 57. Croll, T. I. ISOLDE: a physically realistic environment for model building into low-
935 resolution electron-density maps. *Acta Crystallogr. Sect. D: Struct. Biol.* **74**, 519–530
936 (2018).
937 58. Emsley, P., Lohkamp, B., Scott, W. G. & Cowtan, K. Features and development of
938 Coot. *Acta Crystallogr. Sect. D* **66**, 486–501 (2010).
939 59. Afonine, P. V. *et al.* Real-space refinement in PHENIX for cryo-EM and
940 crystallography. *Acta Crystallogr. Sect. D* **74**, 531–544 (2018).
941 60. Chen, V. B. *et al.* MolProbity: all-atom structure validation for macromolecular
942 crystallography. *Acta Crystallogr. Sect. D* **66**, 12–21 (2010).
943 61. Kabsch, W. XDS. *Acta Crystallogr. Sect. D* **66**, 125–132 (2009).
944 62. Evans, P. R. An introduction to data reduction: space-group determination, scaling
945 and intensity statistics. *Acta Crystallogr. Sect. D: Biol. Crystallogr.* **67**, 282–292 (2011).
946 63. Agirre, J. *et al.* The CCP4 suite: integrative software for macromolecular
947 crystallography. *Acta Crystallogr. Sect. D, Struct. Biol.* **79**, 449–461 (2023).

64. Habermann, B. The BAR-domain family of proteins: a case of bending and binding? *EMBO Rep.* **5**, 250–255 (2004).
65. Terwilliger, T. C. *et al.* Decision-making in structure solution using Bayesian estimates of map quality: the PHENIX AutoSol wizard. *Acta Crystallogr. Sect. D* **65**, 582–601 (2009).
66. Skubák, P. *et al.* A new MR-SAD algorithm for the automatic building of protein models from low-resolution X-ray data and a poor starting model. *IUCrJ* **5**, 166–171 (2018).
67. Adams, P. D. *et al.* The Phenix software for automated determination of macromolecular structures. *Methods* **55**, 94–106 (2011).
68. Luo, Z.-Q. & Isberg, R. R. Multiple substrates of the Legionella pneumophila Dot/Icm system identified by interbacterial protein transfer. *Proc. Natl. Acad. Sci.* **101**, 841–846 (2004).
69. Monticelli, L. *et al.* The MARTINI Coarse-Grained Force Field: Extension to Proteins. *J. Chem. Theory Comput.* **4**, 819–834 (2008).
70. Wassenaar, T. A., Ingólfsson, H. I., Böckmann, R. A., Tieleman, D. P. & Marrink, S. J. Computational Lipidomics with insane: A Versatile Tool for Generating Custom Membranes for Molecular Simulations. *J. Chem. Theory Comput.* **11**, 2144–2155 (2015).
71. Berendsen, H. J. C., Postma, J. P. M., Gunsteren, W. F. van, DiNola, A. & Haak, J. R. Molecular dynamics with coupling to an external bath. *J. Chem. Phys.* **81**, 3684–3690 (1984).
72. Bussi, G., Donadio, D. & Parrinello, M. Canonical sampling through velocity rescaling. *J. Chem. Phys.* **126**, 014101 (2007).
73. Parrinello, M. & Rahman, A. Polymorphic transitions in single crystals: A new molecular dynamics method. *J. Appl. Phys.* **52**, 7182–7190 (1981).
74. Kutzner, C. *et al.* GROMACS in the Cloud: A Global Supercomputer to Speed Up Alchemical Drug Design. *J. Chem. Inf. Model.* **62**, 1691–1711 (2022).
75. ŠAli, A. & Overington, J. P. Derivation of rules for comparative protein modeling from a database of protein structure alignments. *Protein Sci.* **3**, 1582–1596 (1994).
76. Jumper, J. *et al.* Highly accurate protein structure prediction with AlphaFold. *Nature* **596**, 583–589 (2021).

77. Grant, B. J., Rodrigues, A. P. C., ElSawy, K. M., McCammon, J. A. & Caves, L. S. D. Bio3d: an R package for the comparative analysis of protein structures. *Bioinformatics* **22**, 2695–2696 (2006).

78. Mi, H. *et al.* Protocol Update for large-scale genome and gene function analysis with the PANTHER classification system (v.14.0). *Nat. Protoc.* **14**, 703–721 (2019).

79. Uhlén, M. *et al.* Proteomics. Tissue-based map of the human proteome. *Sci. (N. York, NY)* **347**, 1260419 (2015).

80. Blanchet, C. E. *et al.* Versatile sample environments and automation for biological solution X-ray scattering experiments at the P12 beamline (PETRA III, DESY). *J. Appl. Crystallogr.* **48**, 431–443 (2015).

81. Panjkovich, A. & Svergun, D. I. CHROMIXS: automatic and interactive analysis of chromatography-coupled small-angle X-ray scattering data. *Bioinformatics* **34**, 1944–1946 (2018).

82. Manalastas-Cantos, K. *et al.* ATSAS 3.0: expanded functionality and new tools for small-angle scattering data analysis. *J. Appl. Crystallogr.* **54**, 343–355 (2021).

83. Guinier, A. La diffraction des rayons X aux très petits angles : application à l'étude de phénomènes ultramicroscopiques. *Ann. Phys.* **11**, 161–237 (1939).

84. Svergun, D. I. Determination of the regularization parameter in indirect-transform methods using perceptual criteria. *J. Appl. Crystallogr.* **25**, 495–503 (1992).

85. Svergun, D. I. Restoring Low Resolution Structure of Biological Macromolecules from Solution Scattering Using Simulated Annealing. *Biophys. J.* **76**, 2879–2886 (1999).

86. Svergun, D., Barberato, C. & Koch, M. H. J. CRYSOL– a Program to Evaluate X-ray Solution Scattering of Biological Macromolecules from Atomic Coordinates. *J. Appl. Crystallogr.* **28**, 768–773 (1995).

Figures

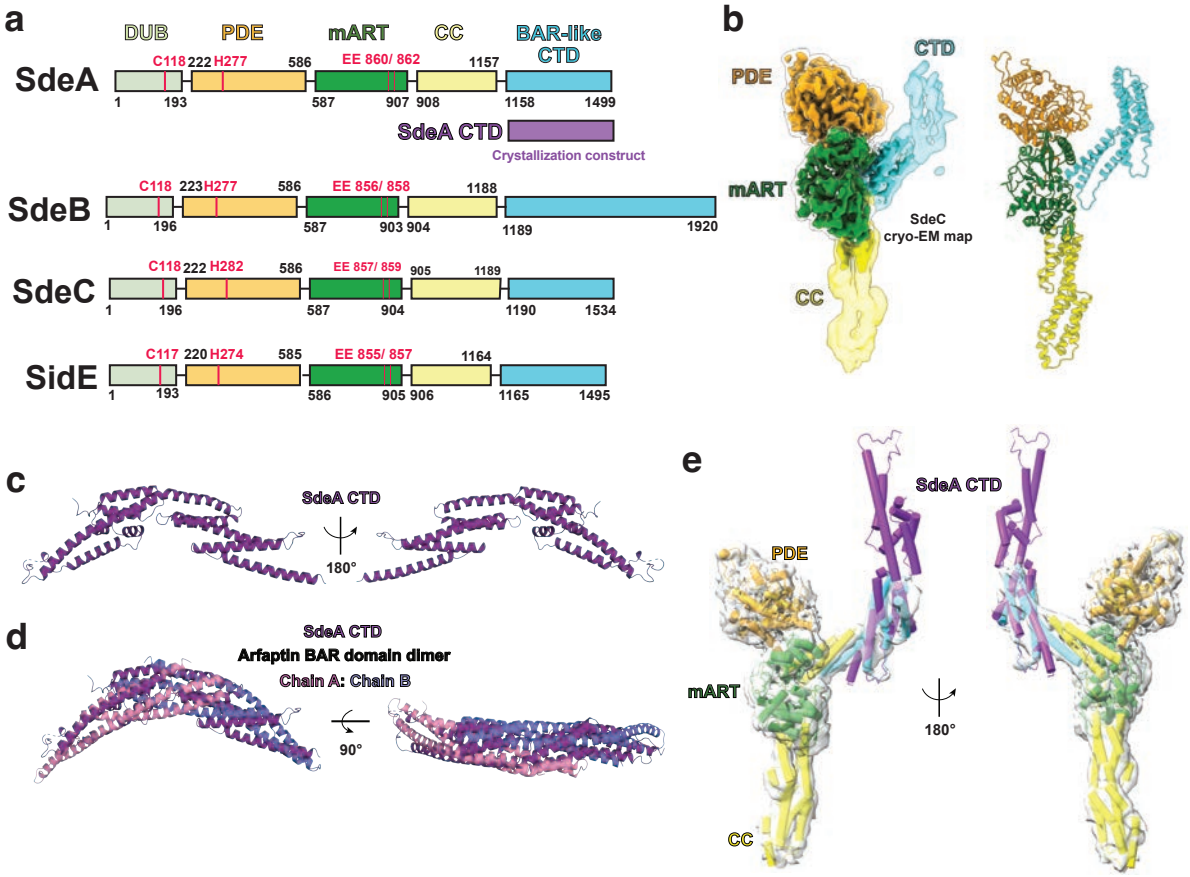

Fig. 1| Structural overview of SidE family members. a, Domain architecture of SidE family: SdeA, SdeB, SdeC and SidE. b, Cryo-EM map obtained for full-length SdeC particles and the corresponding model. c, Crystal structure of SdeA C-terminal domain. d, Overlay of Arfaptin N-BAR dimer with SdeACTD monomer. e, Integrative model of SdeC cryo-EM model and SdeA CTD crystal structure providing a snapshot of the overall spatial arrangement of SidE domains.

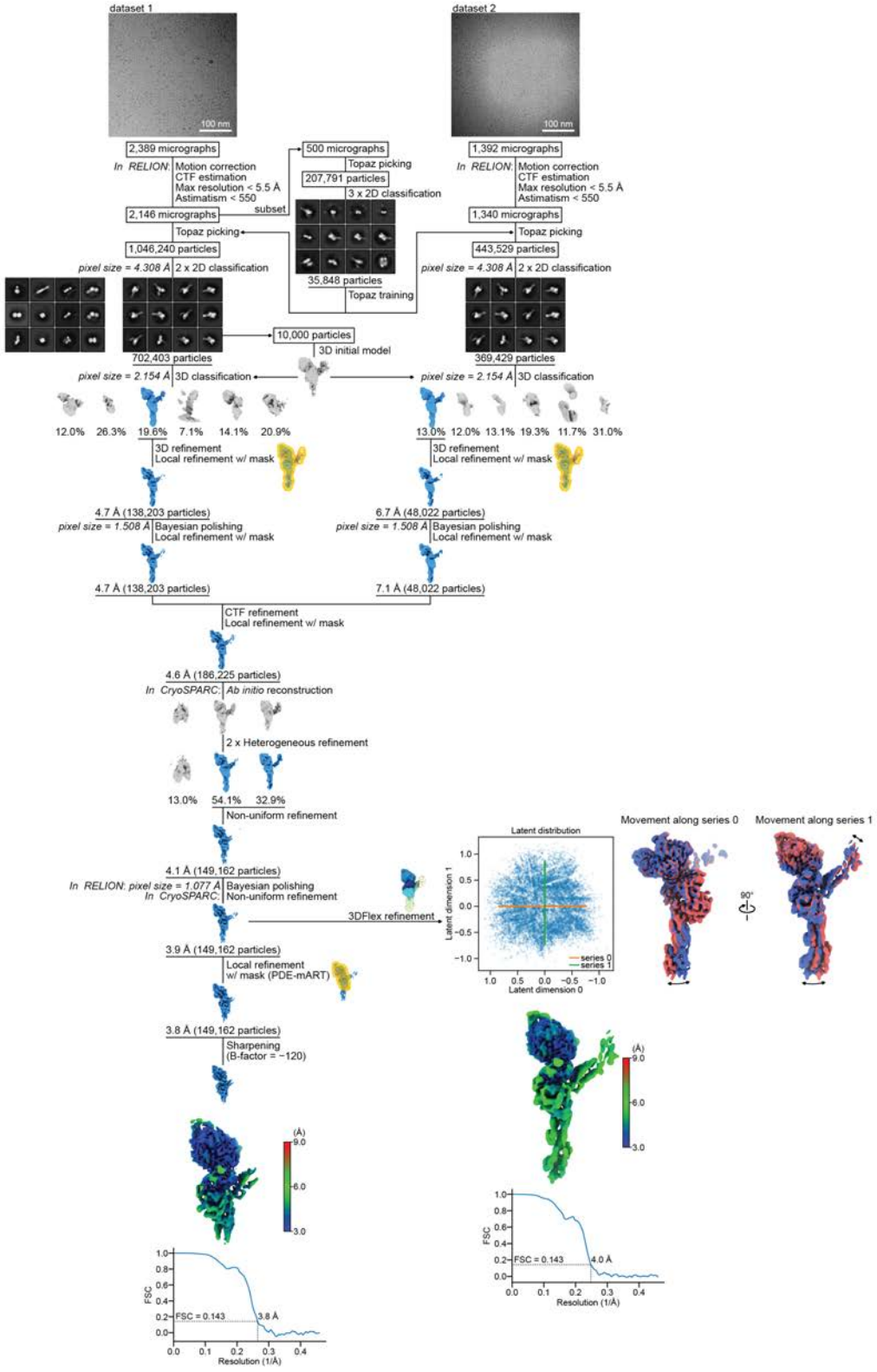

Extended Data Fig.1| Data processing pipeline for the two datasets collected for full-length SdeC particles.

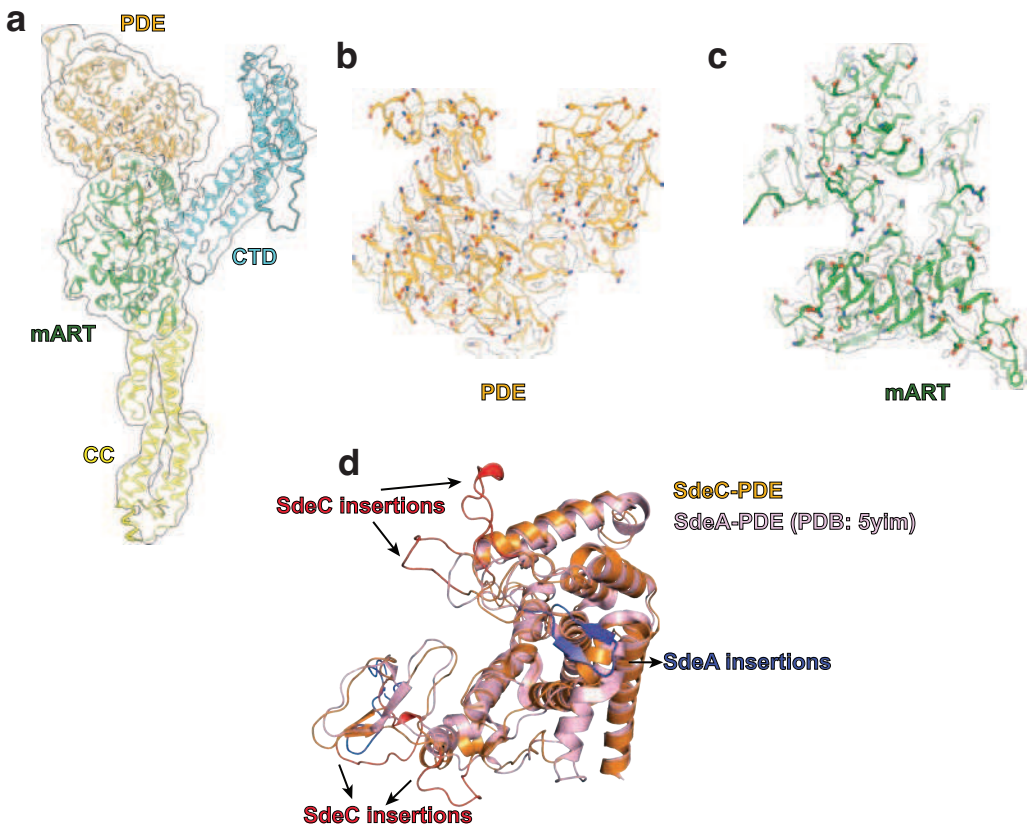

Extended Data Fig. 2| Cryo-EM envelopes for SdeC particles. a, EM-map of the full-length SdeC molecules representing PDE in orange, mART in green, coiled-coil in yellow and CTD in cyan. Focus refined maps for b, PDE domain, and c, mART domain to demonstrate high-confidence model building into the EM maps. d, superposition of SdeC PDE derived from cryo-EM model and SdeA PDE from crystal structure (PDB: 5yim).

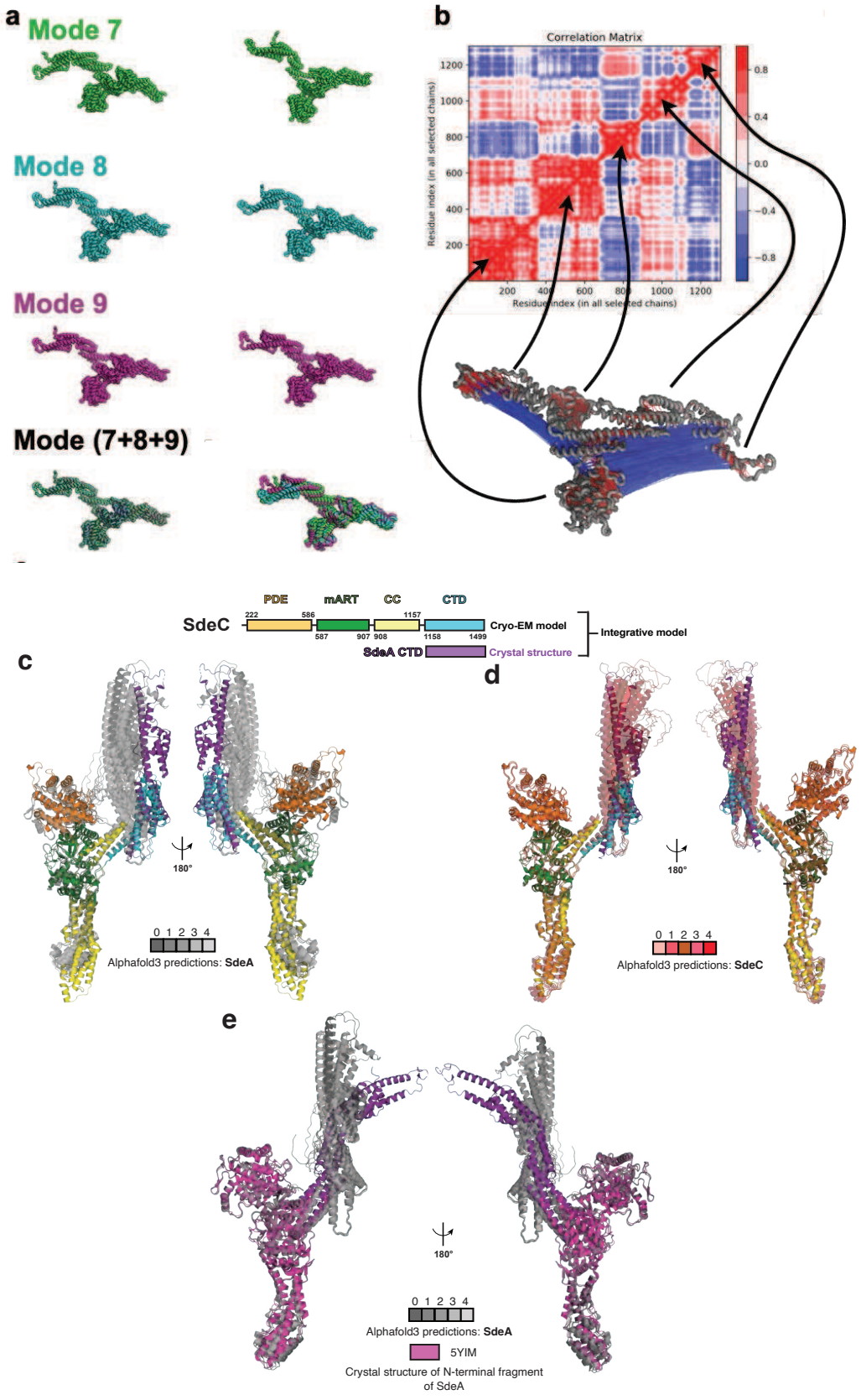

Extended Data Fig. 3| Inherent flexibility of full-length SdeC structure. A, Extreme conformations corresponding (left-to-right) to the three lowest frequency normal modes (green, blue and purple) computed with the full-length SdeC structure (AF model). **b**,

Correlation motions along these modes are plotted as a correlation matrix along the SdeC sequence. Edges joining Cα atoms of SdeC represent the elastic network and coupled (red edges, mostly intra-domain Cα pairs) and uncoupled residue motions (blue edges, mostly inter-domain Cα pairs) quantifying the overall flexibility of SdeC. Superimposition of the SdeC integrative model with corresponding Alphafold3 predictions of c, SdeA d, SdeC. e, Composite model of SdeA crystal structures and its comparison with Alphafold3 predictions of SdeA.

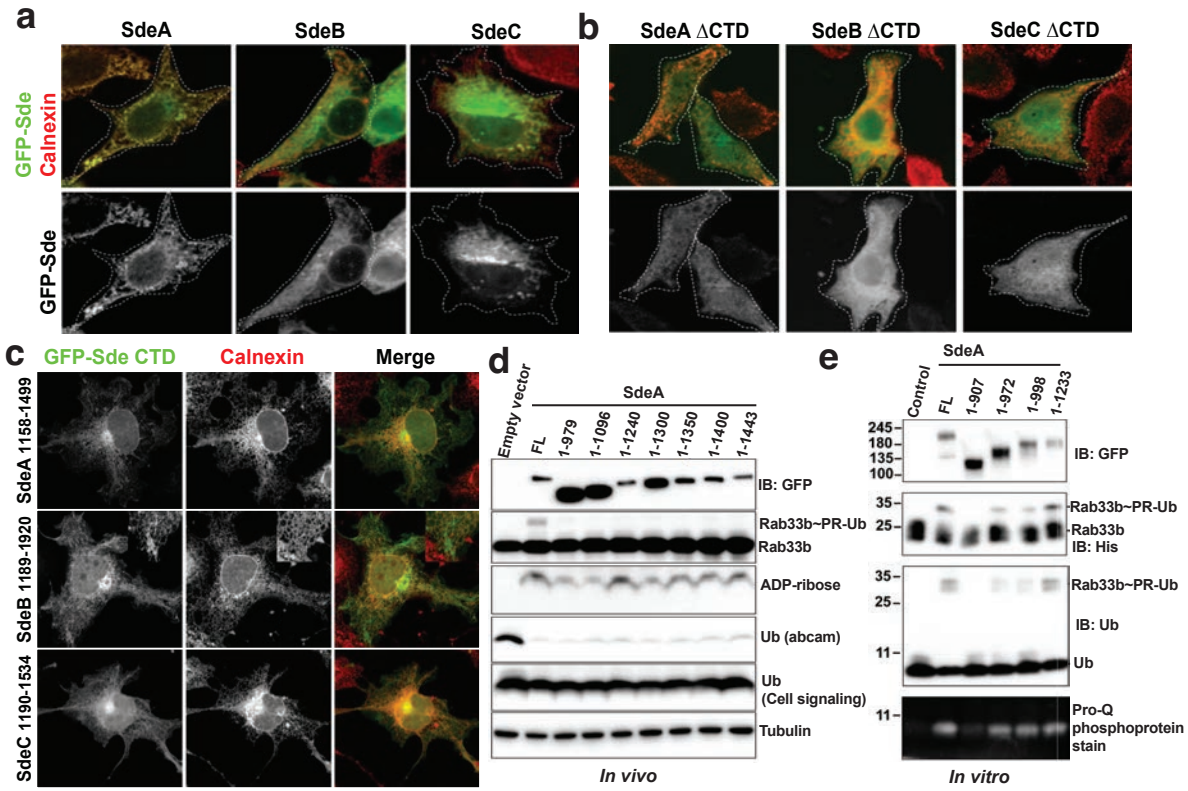

Fig. 2| SidE CTD determines its localization and substrate specificity. a, Colocalization of SdeA, SdeB and SdeC with ER marker calnexin shows its localization to membrane compartments. b, Deletion of the CTD of SdeA, SdeB and SdeC abrogates ER localization. c, SdeA, B, C CTD minimal constructs colocalize with calnexin. d, Upon transfection into cells, C-terminal deletions of SdeA cannot perform PR-ubiquitination of Rab33b as a substrate. e, *In vitro*, the purified C-terminal truncation constructs are capable of catalyzing Rab33b PR-ubiquitination.

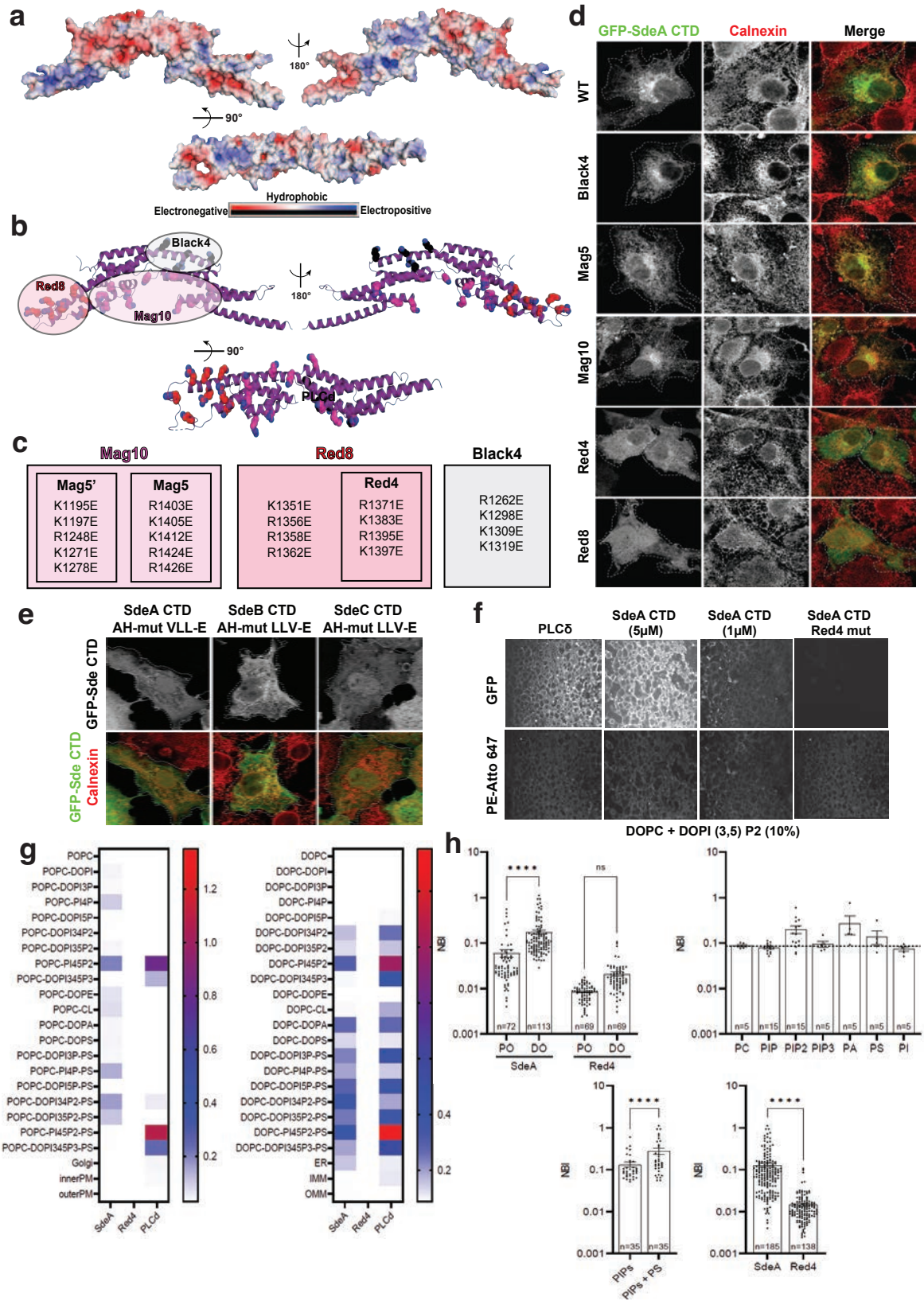

Fig. 3| Dissection of the membrane binding site of SidE CTDs. a, Electrostatic surface view of SdeA CTD shows the electropositive, electronegative, and hydrophobic patches. b, Selection of electropositive patches as probes for membrane-interacting regions. c, Overview

of the mutations designed for each electropositive patch named as Mag10, Red8, and Black4. d, Evaluation of calnexin colocalization of SdeA CTD mutants as a measure for their membrane binding activity. e, Mutational analysis of the three hydrophobic residues from the predicted amphipathic helices from SdeA, SdeB and SdeC reveals loss of membrane engagement. f, LiMA assay used to evaluate *in vitro* binding of EGFP-SdeA CTD and Red4 mutant. The PH domain of PLCδ, known to recognize PI(4,5)P_2, is used as a positive control. f, Representative micrographs showing the colocalization of a marker of liposome membrane, PE-Atto647, with PLCδ and SdeA CTD. g, Heat map for preferred association of SdeA CTD with various liposome compositions either in POPC or DOPC mixtures (white- no binding; blue to red- low to high binding). h-k, Statistical evaluation of preferred liposome compositions for SdeA CTD and the mutant Red4. ****, $p<0.001$. h, Comparison of binding affinities between GFP-SdeA CTD and Red4 mutant for DOPC- (rigid) or POPC-containing (fluid) membranes. i, Comparison of binding affinities of GFP-SdeA CTD for membranes containing various signaling lipids. j, Comparison of binding affinities of GFP-SdeA CTD for PIP-containing membranes and PIP+PS-containing membranes. k, Comparison of all measured binding affinities between GFP-SdeA CTD and its Red4 mutant.

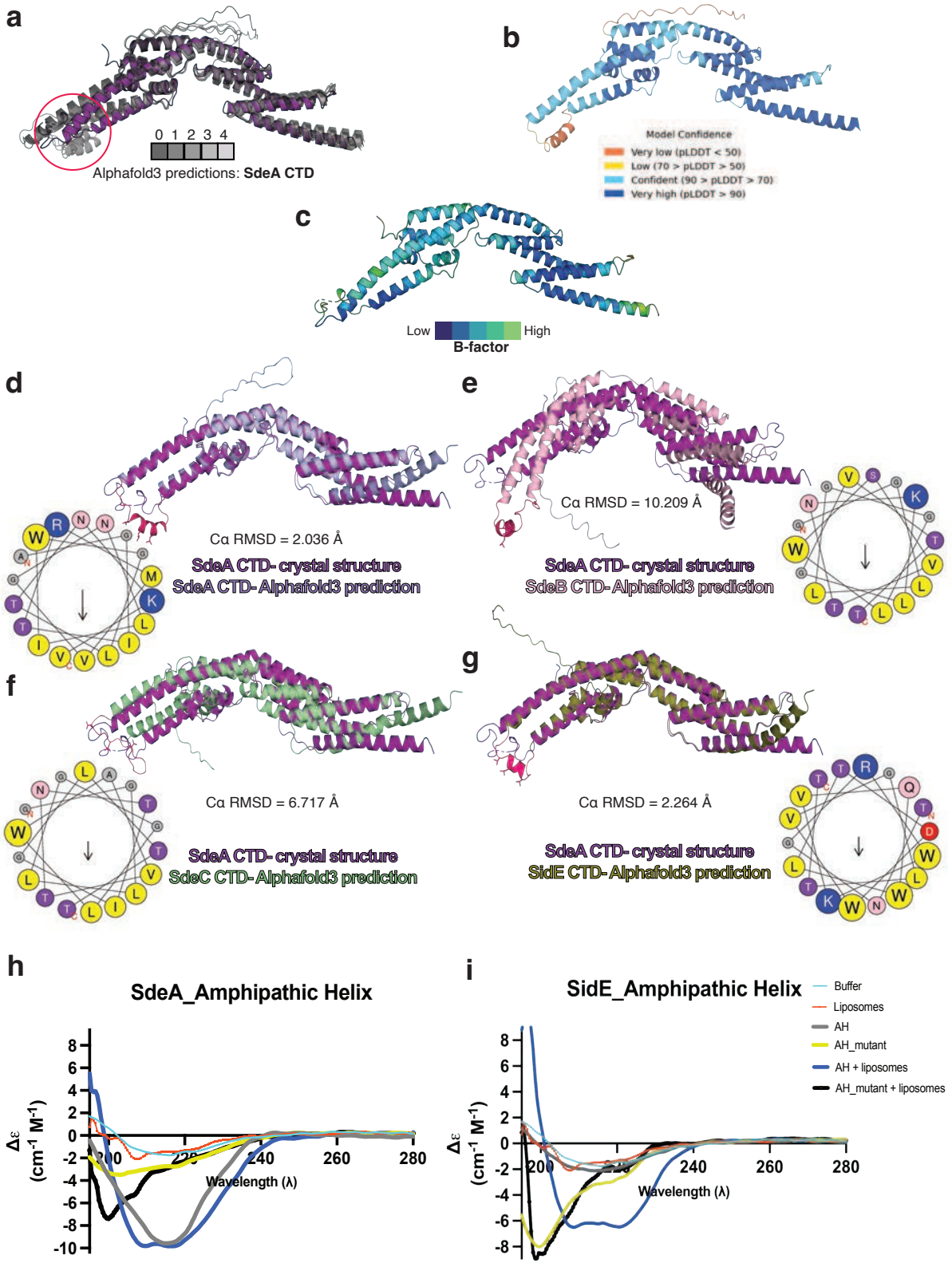

Extended Data Fig. 4| Alphafold predictions of SidE CTD and discovery of amphipathic helix. a, Comparison of SdeA CTD crystal structure with the top 5 AF3 predictions. Three predictions show the presence of a helix in the disordered segment of the X-ray model b,

Mapped pLDDT scores on the AF3 prediction reflecting the confidence of predictions of different regions of SdeA CTD. c, Experimental b-factors from refined crystal structure of SdeA CTD. d, Alphafold3 model of a, SdeA CTD b, SdeB CTD c, SdeC CTD and d, SidE CTD superimposed with SdeA CTD crystal structure and the prediction of amphipathic helix highlighted in red with corresponding Heliquest helical wheel diagrams[26]. Circular Dichroism Spectroscopy for the amphipathic peptides derived from e, SdeA CTD, and f, SidE CTD.

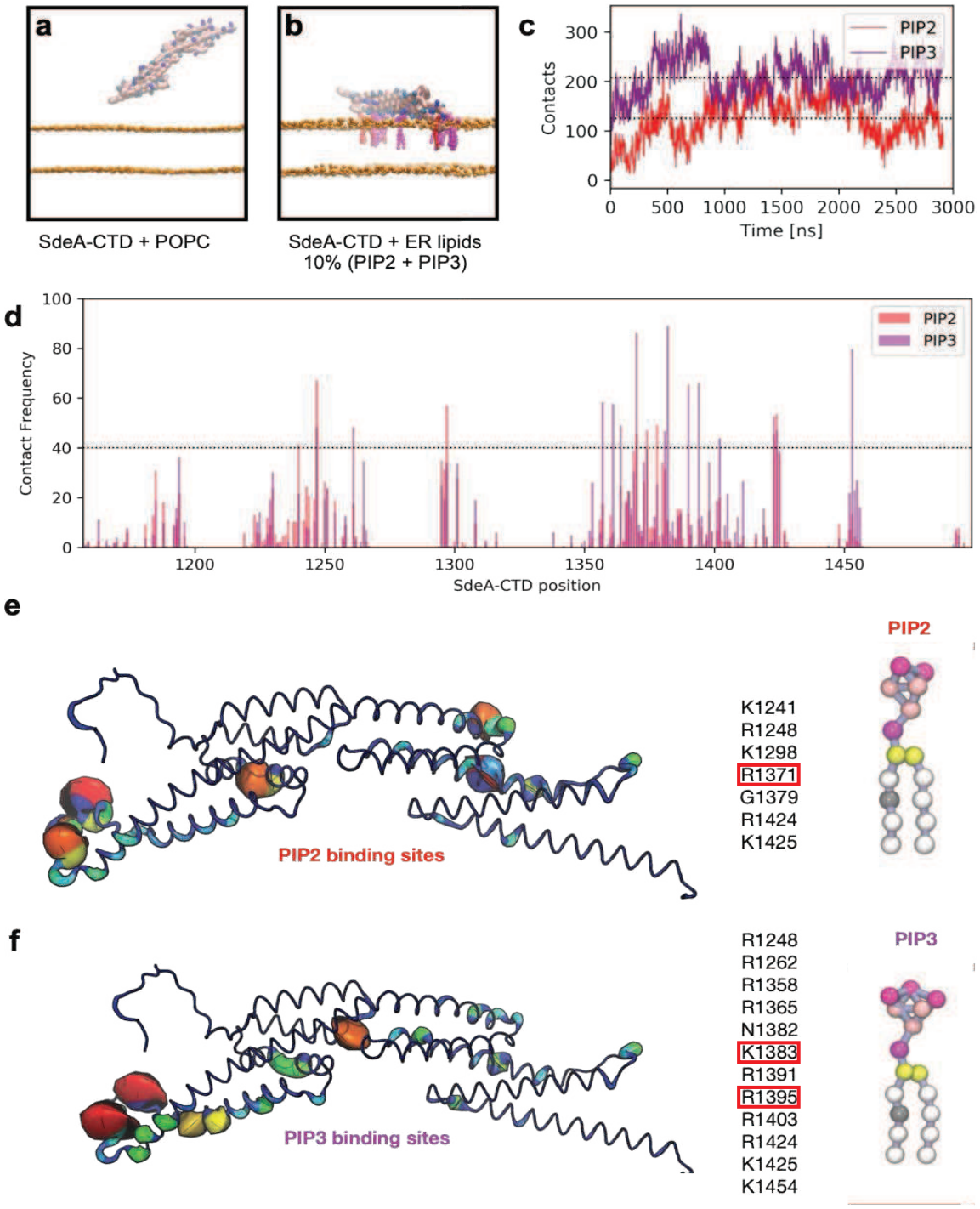

Extended Data Fig. 5| Molecular simulations capture PIP binding sites on SdeA-CTD. Representative snapshots from coarse-grained MD simulations of SdeA-CTD using the MARTINI model in the presence of **a**, pure POPC bilayer, and **b**, bilayer doped with 10% PIP lipids, show the importance of long-range electrostatic interactions for the recruitment of SdeA-CTD to the membrane surface. **c**, Time series of SdeA-CTD–PIP2 (red) and SdeA-CTD–PIP3 (purple) contacts. **d,** The frequency of PIP contacts computed for all CTD residues enabled the mapping of **e,** PIP2 and **f**, PIP3 binding sites. Residues mediating a high number of

contacts are shown as B-factors on the protein main-chain and also highlighted on the right. Residues that overlap with the Red4 mutations in Figure 3c are boxed with a red outline.

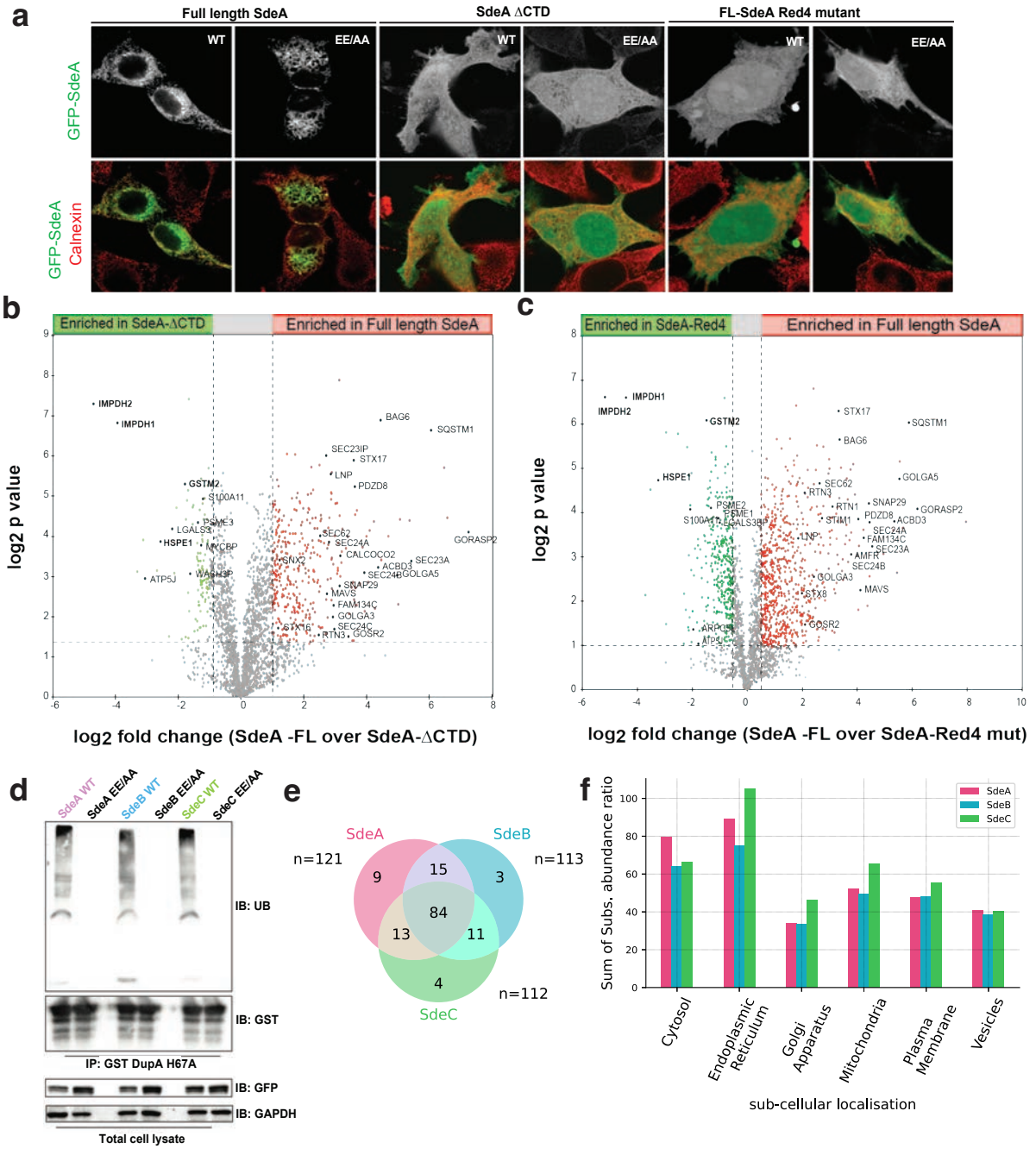

Fig. 4| SdeA CTD is required for its substrate specificity. a, Colocalization of full-length SdeA and its catalytically inactive form EE/AA with calnexin and its comparison with the ΔCTD construct and membrane-binding defective Red4 mutant. Mass-spectroscopy-based determination of substrates of SdeA full-length and its b, ΔCTD, or c, Red4 mutant counterparts. d, DupA pull-downs for over-expressed SdeA, SdeB and SdeC WT and their inactive mutants (EE/AA) to identify substrates for each family member. e, Venn diagram showing the numbers of unique and overlapping substrates for SdeA, SdeB and SdeC, shared

in transfection and infection settings (see Methods). f, Bar plot showing the total abundance of uniquely identified substrates (summated over all proteins) of SidE family members, shared between the transfection and infection settings.

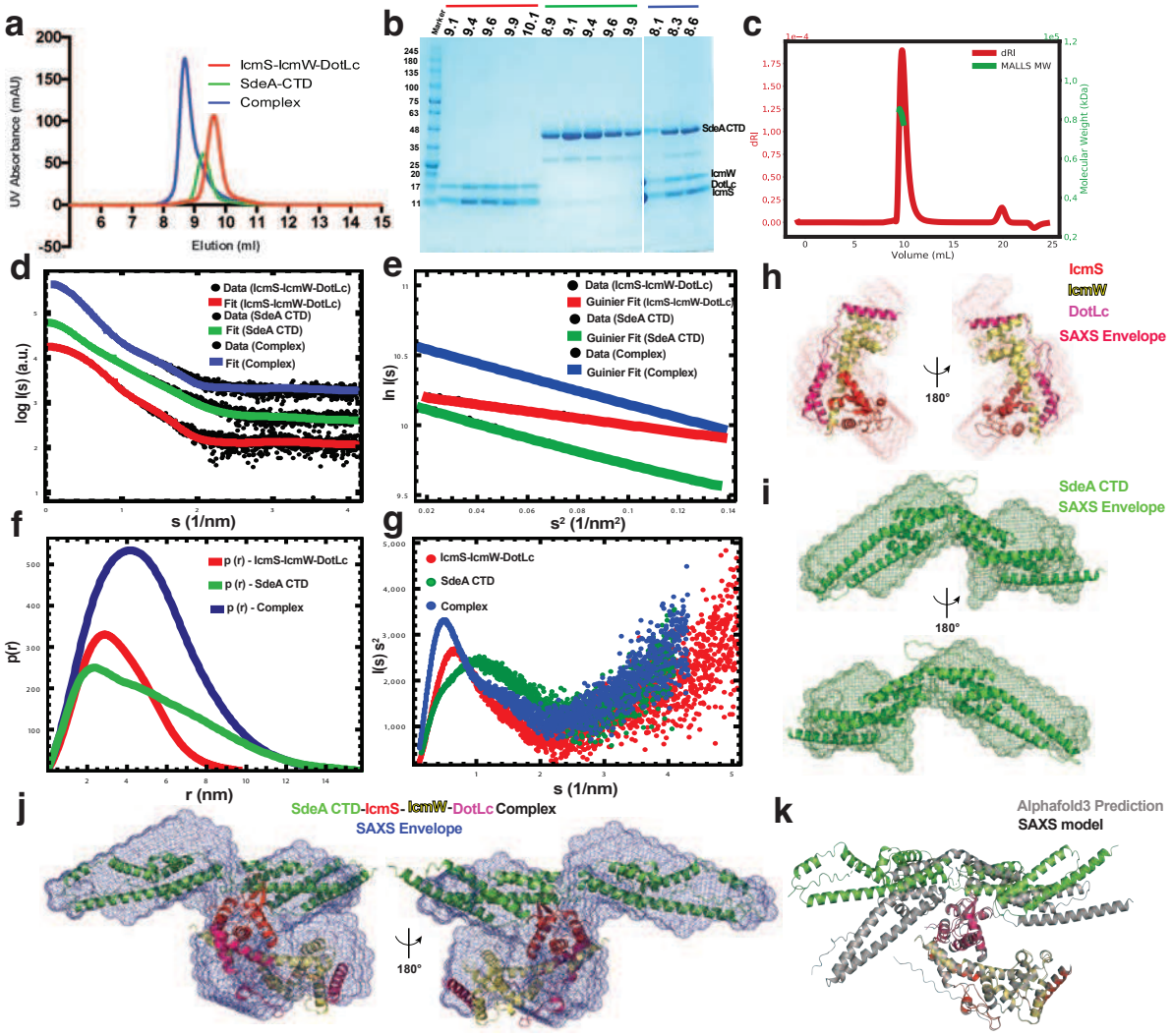

Fig. 5| Biophysical and structural characterization of SdeA CTD interaction with IcmS-IcmW-DotLc complex a, Overlay of the size exclusion profiles of SdeA CTD, IcmS-IcmW-DotLc subcomplex and the holo (SdeACTD-IcmS-IcmW-DotLc) complex. b, SDS-PAGE analysis of the fractions from each size exclusion run with corresponding elution volumes. c, SEC-MALS data of the SdeACTD-IcmSWDotLc complex is represented which confirms the MW as monomer of each protein in the complex. d, SEC-SAXS data from IcmS-IcmW-DotLc, SdeACTD and SdeACTD-IcmS-W-DotLc complex. The overlay for each sample indicates the computed scattering profiles of the NMA-refined Alphafold3 predictions of IcmS-IcmW-DotLc (red) and SdeACTD (green), and of the SdeACTD-IcmSWDotLc complex (blue). The scattering intensity computed from the models fits the experimental data well for all three constructs. e, the Guinier fits of the initial regions to determine the radius of gyration are displayed. f, the distance distribution p(r) functions of the three samples are represented. g,

the Kratky plots indicate compact folded structures of the three samples. The *ab initio* SAXS envelopes (beads) with fitted Alphafold3 predictions of the h, IcmS-IcmW-DotLc i, SdeACTD j, SdeACTD-IcmS-IcmW-DotLc are displayed. k, the superposition of unfitted Alphafold3 model with derived SAXS model shows structural plasticity in SdeA CTD in solution.

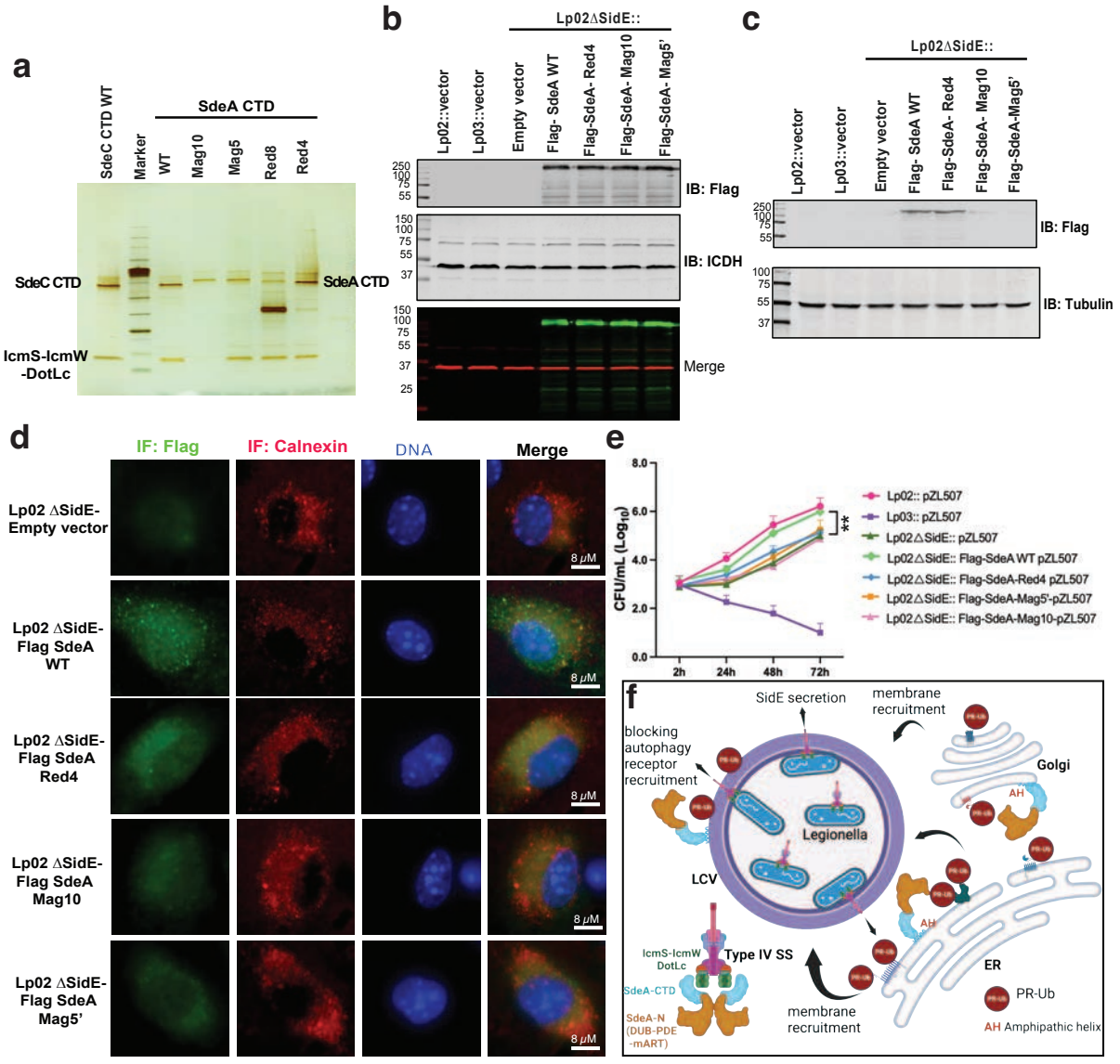

Fig. 6| SdeA CTD has mutually exclusive membrane binding and secretion signal sites. a, Pull-down of IcmS-IcmW-DotLc subcomplex with SdeC CTD, SdeA CTD and its mutants (as shown in Figure 3). b, Expression of WT SdeA and SdeA mutants in Lp02ΔSidE deletion strain of *Legionella*. c, Evaluation of secretion of the WT SdeA and its mutants from *Legionella* into the host. d, Colocalization of WT SdeA and its mutants in macrophages with calnexin as ER marker. e, Growth curves for various strains of *Legionella* including the ones where SidE deletion strain is complemented by either WT SdeA or its mutants. f, Working model of the functional role of SidE CTDs in *Legionella* infection and replication.

Supplementary Files

This is a list of supplementary files associated with this preprint. Click to download.

- Supplementarydata1LiMAcompositions.xlsx